Targeting FSP1 triggers ferroptosis in lung cancer

Katherine Wu[1,2*], Alec J Vaughan[1,2*], Jozef P Bossowski[1,3], Yuan Hao[1,3], Aikaterini Ziogou[1,3], Seon Min Kim[4], Tae Ha Kim[4], Mari N Nakamura[1,3], Ray Pillai[1,5,6], Mariana Mancini[1,3], Sahith Rajalingam[1,3], Mingqi Han[7,8], Toshitaka Nakamura[10], Lidong Wang[9], Suckwoo Chung[1,3], Diane Simeone[9], David Shackelford[7,8], Yun Pyo Kang[4], Marcus Conrad[10, 11], Thales Papagiannakopoulos[1,3#]

[1]Department of Pathology, New York University Grossman School of Medicine, New York, NY, USA.

[2]Vilcek Institute of Graduate Biomedical Sciences, New York University Grossman School of Medicine, New York, NY, USA.

[3]Laura and Isaac Perlmutter Cancer Center, New York University Langone Health, New York, NY, USA.

[4]College of Pharmacy and Research Institute of Pharmaceutical Sciences, Seoul National University, Seoul, Korea

[5]Division of Pulmonary and Critical Care Medicine, Department of Medicine, VA New York Harbor Healthcare System, New York, USA.

[6]Division of Pulmonary, Critical Care, and Sleep Medicine, Department of Medicine, New York University Grossman School of Medicine, New York, USA.

[7]Pulmonary and Critical Care Medicine, David Geffen School of Medicine (DGSOM), University of California Los Angeles (UCLA), Los Angeles, CA, USA.

[8]Jonsson Comprehensive Cancer Center, UCLA, Los Angeles, CA, USA.

[9]Moores Cancer Center, University of California, San Diego, La Jolla, CA, USA

[10]Institute of Metabolism and Cell Death, Molecular Targets and Therapeutics Center, Helmholtz Munich, Neuherberg, Germany.

[11]Translational Redox Biology, Technical University of Munich (TUM), TUM Natural School of Sciences, Garching, Germany.

*These authors contributed equally

#Correspondence to:

Thales Papagiannakopoulos, PhD, thales.papagiannakopoulos@nyulangone.org

Key words: lung cancer, ferroptosis, FSP1, GPX4

ABSTRACT

Pre-clinical and clinical studies have demonstrated how dietary antioxidants or mutations activating antioxidant metabolism promote cancer, highlighting a central role oxidative stress in tumorigenesis. However, it is unclear if oxidative stress ultimately increases to a point of cell death. Emerging evidence indicates that cancer cells are susceptible to ferroptosis, a form of cell death triggered by uncontrolled lipid peroxidation[1-3]. Despite broad enthusiasm about harnessing ferroptosis as a novel anti-cancer strategy, whether ferroptosis is a barrier to tumorigenesis and if it can be leveraged therapeutically remains unknown[4,5]. Using genetically-engineered mouse models (GEMMs) of lung adenocarcinoma (LUAD), we performed tumor specific loss-of-function studies of the two key ferroptosis suppressors, *glutathione peroxidase 4* (*Gpx4*)[6,7] and *ferroptosis suppressor protein 1* (*Fsp1*)[8,9], and observed increased lipid peroxidation and robust suppression of tumorigenesis, suggesting that lung tumors are highly sensitive to ferroptosis. Furthermore, across multiple pre-clinical models, we found that FSP1 was required for ferroptosis protection *in vivo*, but not *in vitro*, underscoring a heightened need to buffer lipid peroxidation under physiological conditions. Lipidomic analyses revealed that Fsp1-knockout ($Fsp1^{KO}$) tumors had an accumulation of lipid peroxides, and inhibition of ferroptosis with genetic, dietary, or pharmacological approaches effectively restored the growth of $Fsp1^{KO}$ tumors *in vivo*. Unlike *GPX4*, *FSP1* expression was prognostic for disease progression and poorer survival in LUAD patients, highlighting its potential as a viable therapeutic target. To this end, we demonstrated that pharmacologic inhibition of FSP1 had significant therapeutic benefit in pre-clinical lung cancer models. Our studies highlight the importance of ferroptosis suppression *in vivo* and pave the way for FSP1 inhibition as a therapeutic strategy in lung cancer patients.

52 **MAIN TEXT**

53 Ferroptosis is a non-apoptotic, oxidative stress-dependent mechanism of cell death that is
54 uniquely distinguished by lipid peroxidation of polyunsaturated fatty acids of membrane
55 phospholipids (PUFA-PL)[1,10]. Lipid peroxidation involves the formation of lipid and lipid peroxyl
56 radicals which, in auto-oxidative propagation reactions, generate lipid hydroperoxides. Aberrant,
57 unrestricted lipid peroxidation results in altered membrane integrity, cell swelling, and ultimately
58 membrane rupture[11,12]. In recent years, growing interest in ferroptosis has elucidated that cells
59 depend on several enzymes to protect against ferroptosis[6-9,13-15], of which Glutathione Peroxidase
60 4 (GPX4) and Ferroptosis Suppressor Protein 1 (FSP1) are the most notable. GPX4 catalyzes the
61 reduction of PUFA-PL hydroperoxides to non-toxic alcohols. FSP1 catalyzes the reduction of
62 extramitochondrial Coenzyme Q_{10} (CoQ), a highly potent lipid radical-trapping antioxidant
63 (RTA). On the other hand, cells can be sensitized to ferroptosis through PUFA-PL composition[16]
64 and biosynthesis by Long-chain Acyl-CoA Synthase 4 (ACSL4)[17-19]. Apart from these cellular
65 pathways, exogenous lipid RTAs, such as liproxstatin-1 (LIP1), ferrostatin-1 (FER1), Vitamin E
66 (VitE), and Vitamin K (VitK), have also been shown to specifically inhibit ferroptosis[1,6,20-22].

67 Emerging evidence indicates that cancer cells, including drug-resistant cells that have
68 adopted a mesenchymal state[2,3], are highly sensitive to lipid peroxidation *in vitro*, garnering
69 excitement about harnessing ferroptosis as a novel anti-cancer strategy. Though there have been
70 extensive studies characterizing GPX4 and more recently FSP1 in various diseases[4,23], whether
71 ferroptosis constitutes a barrier to tumorigenesis and the functional roles of GPX4 and FSP1 in *in*
72 *vivo* cancer models remain poorly characterized. To date, FSP1 has been shown to be a critical
73 ferroptosis suppressor only in the absence of GPX4[8,9,24]. However, given the high toxicity, poor
74 selectivity, and low to limited bioavailability of GPX4 inhibitors *in vivo*[25,26] as well as the only

75 recent development of FSP1 inhibitors, the majority of which do not have *in vivo* efficacy[9,24,27-30],
76 much work remains to demonstrate that ferroptosis induction could indeed be a therapeutic strategy
77 for cancer[5].

78 Here we show that genetic knockout of either Gpx4 or Fsp1 in genetically-engineered
79 mouse models (GEMMs) of autochthonous Kras-driven lung adenocarcinoma (LUAD)[31-35] results
80 in dramatic restriction of lung tumorigenesis. We demonstrate that disruption of Fsp1, often
81 considered a backup axis of ferroptosis suppression, is unexpectedly sufficient to trigger exhibit
82 enhanced lipid peroxidation in lung tumors. We confirm that Fsp1 deletion across several human
83 cancer cell lines with various oncogenic drivers, co-mutations, and tissue lineages consistently
84 lead to *in vivo* tumor restriction. As ferroptosis can be functionally defined as a modality of cell
85 death resulting from elevated lipid peroxides and rescued only with inhibitors of lipid peroxidation,
86 we demonstrate that Fsp1-knockout ($Fsp1^{KO}$) tumors have increased oxidized PUFA-PLs and that
87 administration of lipid RTAs, as well as genetic loss of Acsl4, effectively restores lung
88 tumorigenesis. Finally, we report that FSP1 is upregulated as LUAD tumors progress and show
89 that FSP1 inhibition suppresses tumor growth and prolongs survival in multiple pre-clinical cancer
90 models. Thus, our work utilizes novel *in vivo* models to characterize and test ferroptosis induction,
91 particularly via FSP1 perturbation, as a therapeutic approach for lung cancer.

92

93 **GPX4 prevents ferroptosis in lung tumors**

94 GPX4 is considered the primary mediator of ferroptosis suppression that has been shown
95 to be essential across a plethora of murine and human cancer cells[7,26,36,37]. Therefore, we sought to
96 interrogate whether GPX4, and more broadly ferroptosis suppression, is a requirement for lung
97 tumorigenesis *in vivo*. Using a well-established GEMM of LUAD ($Kras^{LSL\text{-}G12D/+}$, $Tp53^{fl/fl}$,

98 *Rosa26*$^{LSL\text{-}Cas9/LSL\text{-}Cas9}$), we initiated Kras$^{G12D/+}$, Tp53$^{-/-}$ (KP) tumors by intratracheal delivery of
99 lentiviruses expressing CRE-recombinase and dual sgRNAs[38] against either Gpx4 (sg*Gpx4*) or
100 non-targeting control (sg*Neo*), enabling CRISPR/Cas9-mediated Gpx4-knockout (Gpx4^{KO}) or
101 wildtype (WT) control tumors, respectively. Concurrently, we treated a cohort of animals with
102 each tumor genotype with Liproxstatin-1 (LIP1), a potent lipid RTA and ferroptosis inhibitor,
103 throughout the entire course of tumorigenic progression (Fig. 1a). Tumor-specific Gpx4 deletion
104 (sg*Gpx4*) led to a significant decrease in lung tumor burden that was not observed in sg*Gpx4*
105 tumor-bearing mice treated with LIP1 (Fig. 1b-d). Efficient Gpx4 deletion was verified by
106 immunohistochemistry (IHC), with less than 15% of tumors in the in sg*Gpx4* group still staining
107 positive for Gpx4 (Extended Data Fig. 1a). IHC for 4-hydroxy-2-noneal (4-HNE), a marker for
108 lipid peroxidation in tissues (Extended Data Fig. 1b)[20], revealed significantly higher levels of lipid
109 peroxidation in sg*Gpx4* tumors compared to control sg*Neo* lung tumors, which was blunted with
110 LIP1 treatment (Fig. 1e, f).

111 Similar to our *in vivo* observations, CRISPR/Cas9-mediated Gpx4^{KO} in KP LUAD cells
112 resulted in a near complete loss of viability and clonogenicity that was fully rescued by the addition
113 of LIP1 (Extended Data Fig. 1c). Targeted lipidomics to profile oxidized phosphatidylcholine
114 (PCs) and phosphatidylethanolamine (PEs) species in KP LUAD cells treated with RSL3, a
115 covalent Gpx4 inhibitor and ferroptosis inducer, revealed a higher abundance of oxidized
116 phospholipids in RSL3-treated cells that again was decreased in cells treated with concomitant
117 LIP1 (Extended Data Fig. 1d). On the other hand, Gpx4 overexpression (Gpx4^{OE}) in KP LUAD
118 cells had no impact on cell viability or clonogenicity basally (Extended Data Fig. 1e) but did confer
119 greater resistance to ferroptosis *in vitro* (Extended Data Fig. 1f). Similarly, supplementation of KP
120 LUAD cells with sodium selenite (Na_2SeO_3) to increase translation of Gpx4[39], a selenoprotein,

121 resulted in a corresponding boost in Gpx4 expression and enhanced ferroptosis resistance *in vitro*
122 (Extended Data Fig. 1g). Taken together, these results demonstrate that Gpx4 is essential for lung
123 tumors to evade ferroptosis and provide evidence that ferroptosis induction may be an effective
124 anti-cancer strategy.
125
126 **Unlike GPX4, FSP1 is upregulated in LUAD**
127 Given our observation that Gpx4 was required for lung tumorigenesis in a GEMM that
128 closely recapitulates human LUAD development and progression, we next asked whether there
129 was clinical evidence suggesting that ferroptosis regulators in general are altered in lung cancer[40].
130 Although GPX4 expression was modestly increased in *KRAS*-mutant LUAD tumors compared to
131 normal lung tissue, there was no correlation with patient tumor stage or overall patient survival
132 (Extended Data Fig. 1h, i). Concordantly, Gpx4 protein levels also did not change during
133 autochthonous LUAD progression in KP GEMM tumors (Extended Data Fig. 1j).
134 Since GPX4 expression did not appear to correlate with any clinical prognostic factors in
135 *KRAS*-mutant LUAD patients, we next investigated FSP1, a second axis of ferroptosis surveillance
136 (Fig. 2a). We found that FSP1 expression was robustly increased in *KRAS*-mutant LUAD patient
137 tumors compared to normal lung and exhibited a positive correlative trend with higher tumor
138 stages (Extended Data Fig. 2a). Additionally, high FSP1 expression correlated with poor survival
139 in *KRAS*-mutant LUAD patients (Fig. 2b). Unlike Gpx4, Fsp1 protein levels increased temporally
140 as lung tumors progressed from adenomas to adenocarcinomas in KP GEMMs (Figs. 2c, d).
141 Altogether, these findings suggest that FSP1 may constitute a major suppressor of ferroptosis in
142 LUAD and is potentially a more viable therapeutic target than GPX4 for lung cancer patients.

143 Since prior studies have suggested that FSP1 may be regulated by KRAS signaling[41] to
144 further determine whether FSP1 upregulation was specific to *KRAS*-mutant LUAD, we stratified
145 LUAD patients by major oncogenic mutations. Again, *FSP1* was robustly increased in tumors
146 relative to normal lung, and this upregulation was observed irrespective of driver mutation or
147 *KRAS* variant (Extended Data Fig. 2b, c). Although *FSP1* expression was more robustly
148 upregulated in *KRAS*-mutant tumors compared to *EGFR*-mutant tumors, LUAD tumors with
149 neither mutation also exhibited upregulation of *FSP1* to the same extent as *KRAS*-mutant tumors.
150 Next, we investigated whether MAPK/ERK pathway regulates FSP1 expression. Both *in vitro*
151 pathway inhibition with RMC-042, a pan-RAS inhibitor, in a panel of *KRAS*-mutant LUAD cell
152 lines as well as multi-immunofluorescence (IF) for co-expression of Fsp1 and pErk in KP GEMM
153 tumors revealed a lack of correlation between FSP1 expression and ERK activation (Extended
154 Data Fig. 2d, e). Thus, these data indicate that *FSP1* expression, at least in the context of LUAD,
155 may not be exclusively dependent on KRAS-mediated oncogenic signaling.
156 Given that patients with *KRAS*-mutant LUAD tumors often have concomitant mutations in
157 *STK11* and *KEAP1*, which portend more advanced disease and poorer prognosis[34,43], we also
158 wondered whether *FSP1* expression was impacted by these mutations. We observed that *FSP1*
159 was significantly increased in LUAD tumors with co-mutation of either *STK11* or *KEAP1*
160 (Extended Data Fig. 2f). Additionally, treatment of a panel of human LUAD cell lines with an
161 NRF2 activator, KI696, led to significantly increased *FSP1* gene expression (Extended Data Fig.
162 2g). Of note, these findings are in accordance with recent studies describing a role for NRF2, which
163 is activated by *KEAP1* mutations, in FSP1 upregulation[42].
164
165 **Fsp1 is required for lung tumorigenesis**

166 To systematically investigate the functional role of Fsp1 in lung cancer, we initiated
167 autochthonous KP LUAD tumors, this time with tumor-specific CRISPR/Cas9-mediated deletion
168 of either Fsp1 or Gpx4 (Fig. 2e). Strikingly, we found that genetic deletion of Fsp1 (sg*Fsp1*) in
169 KP LUAD tumors strongly suppressed lung tumorigenesis, resulting in significantly decreased
170 tumor burden to the same extent as Gpx4^{KO} (sg*Gpx4*) tumors (Fig. 2f, g). Efficient Fsp1 deletion
171 was verified by immunohistochemistry (IHC), with less than 5% of tumors in the in sg*Fsp1* group
172 still staining positive for Fsp1 (Extended Data Fig. 3a). We did not observe significant changes to
173 the total number or size of tumors formed across the three biological groups (Extended Data Fig.
174 3b, c), which suggested that loss of Fsp1 or Gpx4 primarily impacts tumor progression rather than
175 tumor initiation. We also observed that Fsp1 or Gpx4 deletion resulted in higher proportions of
176 adenomas to adenocarcinomas compared to control tumors (Fig. 2h), indicating that Fsp1 and
177 Gpx4 are functionally important for malignant disease progression. Additionally, there were no
178 notable changes to tumor cell proliferation or apoptotic cell death (Extended Data Figs. 3d, e) in
179 sg*Fsp1* or sg*Gpx4* tumors. In contrast, TUNEL staining of lung tumors demonstrated increased
180 cell death with Fsp1 loss (Fig. 3l), suggesting that the decreased lung tumor burden with Fsp1 or
181 Gpx4 genetic deletion is likely due to increased tumor cell ferroptosis. Perhaps most exciting
182 though is the extent to which Fsp1 deletion phenocopied Gpx4 loss *in viv*o, as this phenotype, to
183 our knowledge, has not yet been reported in any other cell lines, tissues, or disease models.
184

185 **Fsp1 is required uniquely *in vivo***

186 The discovery of FSP1 as a key regulator of ferroptosis arose from genetic screens to
187 identify ferroptosis suppressors in the absence of functional GPX4[8,9]. Thus, FSP1 is generally
188 thought to control a secondary anti-ferroptotic axis whose function, at least *in vitro*, is masked

189 when GPX4 is intact. Accordingly, we observed that CRISPR/Cas9-mediated Fsp1 deletion in KP
190 LUAD cells had no impact on cell viability and clonogenicity *in vitro* (Fig. 2i, Extended Data Fig.
191 4a). As expected, Fsp1-knockout ($Fsp1^{KO}$) cells were more sensitive to RSL3 treatment than
192 isogenic Fsp1-wildtype ($Fsp1^{WT}$) cells and protected from RSL3-killing by LIP1 (Fig. 2j). Despite
193 the remarkable restriction of KP LUAD tumorigenesis by Fsp1 loss *in vivo*, our *in vitro* studies
194 indicated in contrast that Fsp1's anti-ferroptotic function was not required by KP LUAD cells in
195 the presence of Gpx4.

196 We sought to dissect this intriguing dichotomy and better understand the distinct *in vivo*
197 dependency of lung tumors on Fsp1. We first performed a series of syngeneic transplantation
198 experiments using isogenic KP, $Fsp1^{KO}$ and $Fsp1^{WT}$ cell lines with no proliferation differences *in*
199 *vitro* to systematically characterize the impact of Fsp1 loss on tumor growth and further interrogate
200 whether Fsp1-mediated tumor differences were specific to *in vivo* growth conditions (Fig. 2i,
201 Extended Data Fig. 4b). Consistently, we found that $Fsp1^{KO}$ cells formed significantly smaller
202 tumors in both immunocompetent subcutaneous xenografts (Extended Data Fig. 4c, d) as well as
203 orthotopic lung tumors (Fig. 2k, Extended Data Fig. 4e, f). Robust suppression of $Fsp1^{KO}$
204 orthotopic lung tumor growth was similarly observed in immunodeficient athymic (NU/J) mice
205 (Extended Data Fig. 4g), as well as in an immunogenic mouse model[43] (Extended Data Fig. 4h).
206 We also observed the same phenotype in age- and sex-matched Fsp1 wildtype versus Fsp1
207 knockout mice (Extended Data Fig. 4i). These studies collectively provide strong evidence that
208 Fsp1's pro-tumorigenic effect is primarily cell-intrinsic. Fsp1 overexpression ($Fsp1^{OE}$) in KP
209 LUAD cells exhibited no *in vitro* growth advantage (Extended Data Fig. 4j) but had enhanced
210 resistance to RSL3-killing (Extended Data Fig. 4k) and accelerated growth of xenograft tumors *in*
211 *vivo* (Extended Data Fig. Fig. 4l, m). Altogether, these results suggest that Fsp1 is essential for

212 LUAD cells' survival *in vivo* and that increased Fsp1 expression is sufficient to promote *Kras*-
213 mutant tumorigenesis *in vivo*.
214
215 **FSP1 dependency is not mutation-specific**
216 To more thoroughly interrogate the functional importance of Fsp1 for tumorigenesis and
217 the translational potential for targeting Fsp1 in cancer, we assessed the requirement of FSP1 for
218 growth of xenograft tumors from human LUAD cell lines harboring a variety of driver mutations,
219 including *KRAS, NRAS, EGFR, TP53, STK11* and *KEAP1*. We found that CRISPR/Cas9-mediated
220 FSP1 genetic deletion consistently and markedly decreased tumor growth in all models tested.
221 Specifically, $Fsp1^{KO}$ (sg*FSP1*) in H2009 (*KRAS*, *TP53* mutant), H1299 (*NRAS*, *TP53* mutant), PC9
222 and H1975 (*EGFR, TP53* mutant) LUAD cells led to robust suppression of subcutaneous tumor
223 growth (Fig. 3a-d), but, analogous to aforementioned studies, did not impact proliferation or
224 viability of cells *in vitro*, unless treated with RSL3 (Extended Data Fig. 5a-d). To assess whether
225 *KRAS*-mutant tumors with *STK11* (LKB1) and/or *KEAP1* mutation also depend on FSP1, we
226 performed CRISPR/Cas9-mediated FSP1 deletion in A549 (*KRAS, KEAP1, STK11* mutant) and
227 16645 (*Kras* mutant, *Stk11*-null) LUAD cells. Again, we observed a dependency for FSP1 *in vivo*
228 (Fig. 3e, f) but not *in vitro* (Extended Data Figure 5e-f). Together these data provide further
229 evidence that FSP1 is indeed required for *in vivo* LUAD tumor growth irrespective of driver and
230 co-mutations.
231 Finally, we asked if Kras-driven tumors of a different lineage also exhibited a requirement
232 for Fsp1 *in vivo*. Excitingly, transplantation of pancreatic adenocarcinoma (PDAC) *Kras*, *Tp53*
233 mutant (KPC7) cells with CRISPR/Cas9-mediated Fsp1 deletion also led to a robust tumor
234 suppression *in vivo* (Fig. 3g, Extended Data Fig. 5g), mirroring the phenotype observed

235 consistently in LUAD models and suggesting that FSP1 dependency *in vivo* may extend to other
236 tissue lineages.
237
238 **Ferroptosis inhibition rescues Fsp1 loss**
239 We hypothesized that defective regulation of lipid peroxidation and subsequent induction
240 of ferroptosis was the mechanism underlying FSP1^{KO} tumorigenic suppression. To assess this, we
241 first performed epilipidomic analysis of Fsp1^{WT} and Fsp1^{KO} orthotopic lung tumors and observed
242 that Fsp1^{KO} tumors exhibited increased abundance of oxidized and truncated PC/PE species,
243 indicative of increased cellular lipid peroxidation (Fig. 4a). We then asked whether ectopic
244 overexpression of Fsp1 or Gpx4 (Extended Data Fig. 6a, b) was sufficient to restore the growth of
245 Gpx4^{KO} or Fsp1^{KO} tumors, which would shed light about the capacity for each ferroptosis defense
246 arm to compensate for the loss of the other. Indeed, we found that Fsp1^{OE} and Gpx4^{OE} effectively
247 restored the growth of Gpx4^{KO} and Fsp1^{KO} tumors, respectively (Fig. 4b-c, Extended Data Fig. 6c,
248 d). These data implicated that tumors require extensive buffering capacity against lipid
249 peroxidation and that while Gpx4 and Fsp1 act through distinct pathways, each can compensate
250 for the loss of the other.
251 Mechanistically, Fsp1 has been shown to suppress ferroptosis by reducing CoQ, an
252 endogenous RTA, and this function is dependent on its localization to the plasma membrane. We
253 utilized a LC/MS-based, quantitative method to determine the abundance of CoQ in tumors, which
254 revealed that Fsp1^{KO} tumors had a significantly decreased ratio of reduced CoQ_9H_2 to oxidized
255 CoQ_9 (Fig. 4d). This decreased ratio was not present in genotypically matched cells at baseline *in*
256 *vitro*, but interestingly upon treatment with RSL3, Fsp1^{KO} cells mimicked the decreased
257 CoQ_9H_2/CoQ_9 observed in tumors. Prior studies have described that mutation of the myristoylation

258 sequence that targets FSP1 to the plasma membrane renders FSP1 unable to protect against lipid
259 peroxidation *in vitro*[8,9], which we also observed in KP LUAD cells (Extended Data Fig. 6e, f). We
260 anticipated that expression of this mutant Fsp1 ($Fsp1^{mut}$) would be similarly unable to restore
261 $Fsp1^{KO}$ tumor growth. Indeed, while $Fsp1^{WT}$-restored tumors grew quickly, both $Fsp1^{mut}$ and
262 $Fsp1^{KO}$ tumors had decreased growth (Extended Data Fig. 6g). These data suggest that tumors
263 require Fsp1 enzymatic activity and subcellular localization *in vivo* to specifically buffer against
264 ferroptosis.

265 Next, we asked whether ferroptosis suppression, via several orthogonal approaches
266 including tumor-specific Acsl4 knockout ($Acsl4^{KO}$), dietary VitE supplementation, and LIP1
267 treatment would restore $Fsp1^{KO}$ tumor growth. Loss or inhibition of Acsl4, which limits PUFA-PL
268 supply and restricts lipid peroxidation (Fig. 4e), has previously been shown to be protective against
269 ferroptosis in $Gpx4^{KO}$ cells *in vitro*[17-19]. Therefore, we sought to determine whether genetic
270 deletion of Acsl4 would suppress ferroptosis and rescue the growth of $Fsp1^{KO}$ tumors *in vivo*. We
271 performed CRISPR/Cas9-mediated genetic deletion of Acsl4 (sg*Acsl4*) in isogenic KP, $Fsp1^{KO}$
272 and $Fsp1^{WT}$ cells. We observed that loss of Acsl4 did not impact cell viability but robustly rescued
273 RSL3-induced ferroptosis *in vitro*, in both $Fsp1^{WT}$ and $Fsp1^{KO}$ cells (Extended Data Fig. 6h).
274 Importantly, Acsl4 deletion significantly restored $Fsp1^{KO}$ lung tumor growth *in vivo* (Extended
275 Data Fig. 6i) and mice with Acsl4, Fsp1-double knockout tumors were found to have increased
276 endpoint disease burden (Fig. 4f, Extended Data Fig. 6j) and decreased overall survival (Extended
277 Data Fig. 6k). Furthermore, tumor-specific $Acsl4^{KO}$ led to a basal acceleration of tumor growth
278 (Extended Data Fig. 6i) and decreased overall survival (Extended Data Fig. 6k), suggesting that
279 decreased accumulation of PUFA-PL in lung tumors may also protect against ferroptosis *in vivo*.

280 VitE is nature's premier lipophilic antioxidant and is specifically able to scavenge lipid

281 radicals and protect against ferroptosis (Fig. 4e). Therefore, we decided to test whether dietary
282 VitE supplementation could rescue the growth of Fsp1^{KO} lung tumors. High versus low VitE diets
283 *ad libitum* was provided to animals either before or after tumor initiation (Fig. 4g), and we found
284 that increased dietary VitE accelerated Fsp1^{KO} tumor growth (Fig. 4h, i), with no impact on growth
285 of Fsp1^{WT} tumors (Extended Data Fig. 6l).

286 Lastly, since LIP1 suppressed tumor lipid peroxidation and entirely mitigated the impact
287 of Gpx4 loss on KP LUAD tumorigenesis (Fig. 1b-d), we conducted parallel studies to investigate
288 whether LIP1 also blunts ferroptosis in and restores Fsp1^{KO} tumorigenesis. In the orthotopic lung
289 tumor model, we observed a tendency for Fsp1^{KO} tumors to grow more quickly with daily LIP1
290 administration (Extended Data Fig. 6m). In the KP LUAD GEMM (Extended Data Fig. 6n), which
291 was conducted in accordance with experimental parameters for Gpx4^{KO} GEMM studies, LIP1
292 treatment significantly increased autochthonous Fsp1^{KO} (sg*Fsp1*) tumor burden (Extended Data
293 Fig. 6o). Moreover, sg*Fsp1* tumors stained positively for 4-HNE, which was effectively
294 suppressed by LIP1 treatment (Extended Data Fig. 6p). As observed with VitE supplementation,
295 timing of LIP1 treatment did not appear to have a differential impact, as LIP1 treatment after
296 tumors were already established was equally effective at restoring sg*Fsp1* lung tumorigenesis (Fig
297 4j-l). Altogether, these studies provide clear evidence that LUAD tumors require Fsp1 to protect
298 against ferroptosis *in vivo* and suggest that increased lipid peroxidation is a barrier for tumor
299 growth and progression.

300

301 **FSP1 inhibition extends overall survival**

302 With the growing interest in harnessing ferroptosis to kill tumor cells, several FSP1
303 inhibitors have been developed[9,28], though the majority are effective only *in vitro* against human

304 FSP1 (hFSP1) in the context of GPX4 loss or inhibition (Extended Data Fig. 7a-d). Recently,
305 icFSP1 was developed as the first human FSP1 (hFSP1) inhibitor with *in vivo* stability and
306 efficacy, albeit solely in tumors with concomitant GPX4 loss[24]. Accordingly, we also saw that
307 icFSP1 treatment *in vitro* did not impact cell viability (Extended Data Fig. 7e) unless RSL3 was
308 added (Extended Data Fig. 7f). Given that murine and human FSP1 are highly conserved in
309 sequence and structure, we generated a hybrid tumor model in which hFSP1 was expressed in
310 murine KP, $Fsp1^{KO}$ tumors. We observed that expression of either murine or human FSP1 resulted
311 in similar acceleration of tumor growth compared to $Fsp1^{KO}$ tumors (Extended Data Fig. 7g, h),
312 which indicated that hFSP1 can functionally compensate for mFsp1 *in vivo*.

313 Using this hybrid tumor model, we next tested whether icFSP1 had therapeutic benefit
314 against lung cancer. Excitingly, we found that FSP1 inhibition as a monotherapy improved overall
315 survival of lung tumor-bearing mice, nearly to the extent of genetic Fsp1 deletion (Fig. 5a). To
316 determine whether the therapeutic effect of icFSP1 was indeed due to the induction of ferroptosis,
317 we asked whether LIP1, which we expected to inhibit lipid peroxidation induced by FSP1
318 inhibition, rescued tumor suppression in icFSP1-treated animals. In correlation with the survival
319 data, we observed that icFSP1-treatment significantly decreased tumor growth when compared to
320 vehicle treated animals, and importantly, concomitant LIP1 treatment abrogated the tumor-
321 suppressive effect of icFSP1 treatment (Fig. 5b, Extended Data Fig. 7c). Further, to test whether
322 icFSP1 was exerting an on-target, tumor-specific effect, we repeated the treatment study with an
323 internal control— lung tumors expressing $FSP1^{Q319K}$, a mutant that is resistant to icFSP1 but
324 maintains anti-ferroptotic function (Extended Data Fig. 7a, b). We found that icFSP1 treatment
325 specifically extended overall survival of mice bearing tumors with $hFSP1^{WT}$ but not $hFSP1^{Q319K}$
326 (Fig. 5c), indicating that indeed the tumor suppression seen with icFSP1 treatment was due to

327 inhibitor activity directly on tumor cells.

328 We wondered whether icFSP1 treatment also impacted the tumor microenvironment
329 (TME), but we found no differences in the proportion of total T cells, neutrophils, alveolar, or
330 interstitial macrophages between the treatment groups (Extended Data Fig. 7j). These data further
331 suggest that icFSP1 primarily exerts on-target, tumor-specific effects, though more granular
332 immune profiling is needed to determine the potential impact, and thus potential side effects, of
333 FSP1 inhibition on TME. Finally, we utilized a PDX model (LX465; *KRAS*^{G12D}, *TP53*-mutant) to
334 further assess the therapeutic potential of FSP1 inhibition. Excitingly, we found that icFSP1
335 treatment significantly decreased PDX tumor growth (Fig. 5d), further bolstering the translational
336 potential of targeting FSP1 in LUAD patients. These pre-clinical studies with icFSP1 are the first
337 to demonstrate that FSP1 is a promising therapeutic target, and our work highlight FSP1 inhibition
338 as a novel therapeutic strategy for improving disease outcome in lung cancer patients.

339

340 **DISCUSSION**

341 Cancer is a disease of hyperproliferation, and cancer cells increase their metabolic output
342 to support sustained growth. This occurs at the cost of increased ROS production that can damage
343 macromolecules, such as lipids, and have deleterious effects[44,45]. One such effect is excessive lipid
344 peroxidation of membrane-associated PUFA-PLs, which can lead to ferroptosis, a unique non-
345 apoptotic mechanism of cell death. Through our systematic interrogation of the key mechanisms
346 that regulate aberrant lipid peroxidation *in vivo*, we demonstrated that ferroptosis constitutes a
347 barrier to lung cancer and that lung tumors rely on Gpx4 and uniquely, Fsp1 to overcome
348 ferroptosis and sustain tumorigenesis (Extended Data Fig. 7k, l).

349 Our work specifically highlights the dependence of lung tumors on Fsp1 *in vivo*, even in

350 the presence of functional Gpx4 (Extended Data Fig. 7k). This is the first report of a context where
351 Fsp1 and Gpx4 are independently required for ferroptosis suppression and therefore either can
352 impact disease outcome. Moreover, analysis of GEMM and human lung tumors demonstrated that
353 FSP1 levels increase during tumor progression and correlate with poor survival. In contrast, GPX4
354 levels are ubiquitous in tumors and most tissues. Given that germline $Gpx4^{KO}$ mice are not viable[46],
355 whereas $Fsp1^{KO}$ mice are with no notable physiological defects[20,47,48], the therapeutic window for
356 targeting FSP1 with fewer toxic side effects is expected to be much greater than for GPX4.
357 Furthermore, loss of GPX4 is toxic to T cells which would suppress any anti-tumor immune
358 responses[49,50]. Leveraging this unique requirement for Fsp1 in lung cancer, our studies demonstrate
359 the therapeutic benefit of FSP1 inhibition in promoting ferroptosis and suppressing tumor growth
360 and extending survival as a monotherapy in aggressive pre-clinical lung cancer models. Our
361 studies underscore the value of *in vivo* pre-clinical models in capturing physiologically relevant
362 metabolic dependencies that may be missed *in vitro* and pave the way for developing FSP1
363 inhibitors for clinical testing in lung cancer patients.
364

365 **Methods**

366 *Cell lines*

367 KP LUAD cell lines were obtained from the laboratory of Tyler Jacks. KP, Fsp1^{KO} cell lines were
368 generated by transient transfection of PX458 (Addgene #48138) expressing an sgRNA targeting
369 Fsp1. Single GFP positive clones were selected and Fsp1 loss was validated by western blot. The
370 16645 cell line was developed from Kras^{G12D} LKB1$^{-/-}$ GEMM as previously described.[51] KPC7
371 cells were obtained from the laboratory of Diane Simeone. All cell lines were maintained in
372 DMEM or RPMI 160 (Corning) supplemented with 10% FBS (Sigma Aldrich) and gentamicin
373 (Invitrogen) and were tested for mycoplasma regularly (PlasmoTest, InvivoGen). All mouse cell
374 lines were authenticated by PCR genotyping. All human cell lines used were purchased from
375 ATCC and were authenticated by short-tandem-repeat profiling. Genetic manipulation of cell lines
376 was performed via lentiviral transduction of plasmids, detailed in next section, followed by either
377 puromycin (7ug/mL) or hygromycin (800ug/mL) selection for 1 week.

378

379 *Cloning/lentivirus generation*

380 CRISPR/Cas9-mediated knockout of target genes was achieved by cloning sgRNAs into pLenti-
381 USEC or lentiCRISPRv2-puro vectors, as previously described[31]. In short, backbones were
382 digested with Esp3I (New England Biosciences) and purified with a gel extraction kit (QIAGEN).
383 sgRNAs were designed using CRISPick (Broad Institute), obtained from Integrated DNA
384 Technologies (Coralville, IA), annealed, phosphorylated, Esp3I-digested, and ligated into the
385 purified digested backbones using Quick Ligase (New England Biosciences). Double sgRNA
386 ultramers were designed and generated as previously described[38]. Briefly, ultramers were Gibson
387 assembled to digested pDonor_sU6 (Addgene #69351), Esp3I-digested, and ligated to purified
388 digested backbones. Guide RNA sequences used to make gene knockouts can be found in

389 Supplementary Data 4. Gpx4, mFsp1, and hFSP1 expression plasmids were generated using
390 Gibson assembly of the respective cDNA into pLenti-v2-filler.

391 Lentivirus was generated by co-transfection of HEK293 cells with a viral vector and packaging
392 plasmids psPAX2 (Addgene #12260) and pMD2.G (Addgene #12259) using PEI transfection
393 reagent. Cell supernatant containing lentivirus was collected 72 hours after transfection and
394 filtered through 0.45 µM PVDF filters. For *in vivo* experiments, lentivirus was concentrated by
395 ultracentrifugation at 25,000rpm for 2 hours at 4°C. The viral pellet was resuspended in PBS and
396 stored at -80°C until use. Viral titer was quantified with the use of a Cre-dependent GreenGo
397 reporter cell line. For *in vitro* experiments, media containing virus was collected, filtered, and
398 added directly to recipient cells with polybrene at 8 µg/mL for 48 hours before selection.

399

400 *Mouse models*

401 All mouse experiments described in this study were approved by the NYU Institutional Animal
402 Care and Use Committee (IACUC). Animals were housed according to IACUC guidelines in
403 ventilated caging in a specific pathogen free animal facility. For all mouse studies, ≥ 4 mice were
404 used for each experimental condition. *Kras*$^{LSL\text{-}G12D/+}$; *Tp53*$^{fl/fl}$; *Rosa26*$^{LSL\text{-}Cas9/LSL\text{-}Cas9}$ (KPC
405 GEMMs) were bred as previously described[31-35]. C57BL/6J (JAX strain #000664) mice with the
406 appropriate genotype, aged 8 to 12 weeks were randomly selected to begin tumor initiation studies
407 with pUSEC lentivirus. Care was taken to ensure each experimental arm had an equal number of
408 male and female mice. Mice were intratracheally infected with lentiviruses as described and
409 monitored until experimental endpoint. Tumor burden was quantified by hematoxylin and eosin
410 (H&E) staining and analyzed using QuPath software as a measurement of total tumor area/total
411 lung lobe area. All quantifications were done with investigator blinded to the respective sample

412 genotypes. All transplantation experiments were performed using nude (JAX strain #002019),
413 NOD SCID Gamma (NSG; JAX strain #005557F), C57BL/6J Fsp1-knockout (Conrad group[16]) or
414 C57BL/6J wildtype (JAX strain #000664) mice aged 8 to 12 weeks old. For murine cell xenograft
415 experiments, 100,000 cells in 100µl of phosphate-buffered saline (PBS) were injected
416 subcutaneously into each flank of the mouse. For the xenograft studies in Figure 3 the number of
417 cells injected per flank and whether they were injected with 50:50 PBS and Matrigel (Corning) are
418 indicated as follows: H2009 (2 million cells +Matrigel), H1299 (1 million cells), PC9 (1 million
419 cells), H1975 (2 million cells +Matrigel), A549 (1 million cells), 16645 (500,000 cells), KPC7
420 (250,000 cells). All human cell line xenograft experiments were carried out in male NSG mice
421 unless specified. For the PDX experiment, tumors were implanted subcutaneously in male NSG
422 mice as previously described[34]. Tumors were measured by caliper, and volume was calculated
423 based on 0.5 x length x width^2. The maximum tumor diameter permitted by our IACUC protocol
424 was 2cm, and this was not exceeded in any experiment. For orthotopic lung tumor experiments,
425 100,000 luciferase-expressing cells in 200µl of PBS were injected intravenously into tail vein of
426 male mice unless specified in the legend. Tumor growth was measured by bioluminescence
427 (PerkinElmer IVIS Spectrum In Vivo Imaging System; D-luciferin, PerkinElmer #122799). Data
428 were analyzed using Living Image software.
429
430 *Antioxidant/drug treatments*
431 For LIP1 treatment, mice were dosed with 10 mg/kg Liproxstatin-1 (BOC Sciences) or Vehicle
432 (2% DMSO + 40%PEG300 + 2%Tween80 in sterile H_2O) by intraperitoneal injection for
433 frequency and duration indicated in figure schematics. For icFSP1 treatment, mice were dosed
434 with 50mg/kg icFSP1 (WuXi LabNetwork) or vehicle (45% PEG300 in sterile PBS) by

435 intraperitoneal injection twice daily. High (TD.2108412) and low (TD.210841) irradiated Vitamin
436 E diets were obtained from Inotivco and provided *ad libitum* for length of time indicated in figure
437 legends. In all experiments, mice were randomly assigned to treatment group.
438
439 *Cell clonogenic and viability assays*
440 Cell clonogenic assays were conducted by seeding 2000 cells per well into 12-well dishes
441 (BD/Falcon) in RPMI-1640 media. After 12-16hrs, media containing RSL3 and/or LIP1 were
442 added to wells. After 5 days of growth, plates were washed twice with PBS and stained with 0.5%
443 crystal violet (Fisher Scientific) solution in 20% methanol. Plates were dried, scanned, and crystal
444 violet was quantified by solubilization with 10% acetic acid and measurement of absorbance at
445 592nm by spectrometer (Molecular Devices). Cell viability assays were conducted by seeding
446 2000 cells per well into white-walled, clear-bottom, 96-well plates (Corning) in RPMI-1640
447 media. After 12-16hrs, media containing RSL3, LIP1, and/or FSEN1, iFSP1, or icFSP1 were
448 added. After 3 days, cell viability was assessed by CellTiter-Glo (Promega) and luminescence was
449 measured by spectrometer (Molecular Devices).
450
451 *Immunoblotting*
452 Cells were plated to 75% confluency in a 6-well dish, and the following day cells were lysed on
453 ice with Pierce RIPA buffer (ThermoScientific) containing 1x protease/phosphatase inhibitor
454 cocktail (Thermo Fisher Scientific). Samples were sonicated in cooled 4°C water (12 rounds, 30
455 seconds on and 30 seconds off) and then centrifuged at 14000 rpm at 4°C for 15 minutes. The
456 supernatant was collected, and protein was quantified using the DC Rad Protein Assay kit. Protein
457 was diluted to 1 ug/uL with water and 4x NuPage LDS sample buffer, then boiled at 95°C for 10

458 minutes. 20 ug protein per well was loaded into Invitrogen 4-12% Bis-Tris gels and then
459 transferred onto PVDF membranes using a standard protocol. PVDF membranes were then
460 blocked using 5% BSA in TBST for 60 minutes at room temperature and incubated with primary
461 antibodies in 5% BSA overnight at 4°C. Primary antibodies were obtained as follows: Gpx4
462 (Abcam), Fsp1 (Proteintech), Acsl4 (Santa Cruz Biotechnologies), pERK (Cell Signaling), ERK
463 (Cell Signaling), and Hsp90 (BD Bioscences). The following day, membranes were washed in
464 TBST and incubated with HRP-conjugated secondary antibodies for 1 hour at room temperature.
465 Enhanced chemiluminescent horseradish peroxidase substrate (ThermoScientific SuperSignal
466 West PICO Plus) was added to the membrane for 1 minute, and the resulting membrane was
467 imaged using the General Electric Amersham Imager 680. For gel source data, see Supplementary
468 Data 1.
469
470 *Oxidized lipidomics*
471 For the Gpx4 KO experiment, cells were plated to 75% confluency in 6-well dish. The following
472 day, cells were treated with DMSO, RSL3 (0.5uM), or RSL3(0.5μM) + LIP1(100nM). After 8hrs,
473 cells were collected and washed in an antioxidant solution (PBS containing dibutylhydroxytoluene
474 (BHT; 100 μM) and diethylenetriamine pentaacetate (DTPA; 100 μM)) and centrifuged.
475 Supernatent was discarded and cell pellets were immediately frozen in liquid nitrogen and stored
476 at –80 °C. Frozen samples were sent on dry ice to Wayne State Lipidomics Core for metabolite
477 extraction and LC-MS analysis.
478 Fsp1 WT and KO tumor and cell lipidomic analysis were performed in the lab of Pyo Kang. Fsp1
479 WT and KO cells were plated at 75% confluency in 10 cm plates and treated as stated above. After
480 euthanasia, animals were perfused with the antioxidant solution (+3.8% trisodium citrate),

481 orthotopic tumors were microdissected, frozen in liquid nitrogen and stored at –80 °C. Mouse lung
482 cancer tissues were cryopulverized and extracted with chloroform:methanol (2:1, v/v) at a tissue
483 concentration of 25 mg mL^{-1}. For the cells, 1.0×10^7 cells were extracted by one milliliter of
484 chloroform:methanol (2:1, v/v). EquiSPLASH LIPIDOMIX® internal standard (Avanti Polar
485 Lipids) was added to the extraction solvent at 0.1 µg mL^{-1} per lipid class. Samples were sonicated
486 on ice for 1 min using a VCX 130 probe sonicator (5 s on/off cycles), incubated for 30 min, and
487 centrifuged at 17,000 × g for 20 min at 4 °C. The supernatant was was dried under vacuum (EZ-2
488 Elite, Genevac), reconstituted in 10% of the original volume with isopropanol, and transferred to
489 glass autosampler vials for LC–MS analysis. Chromatographic separation was performed using a
490 Waters ACQUITY UPLC CSH C18 column (100 × 2.1 mm, 1.7 µm) with a VanGuard precolumn
491 (5 × 2.1 mm, 1.7 µm). Mobile phase A consisted of acetonitrile/water (60:40, v/v), and mobile
492 phase B of isopropanol/acetonitrile (90:10, v/v), both containing 5 mM ammonium formate and
493 0.1% formic acid. The column was maintained at 65 °C with a flow rate of 0.6 mL min^{-1}. The
494 gradient was as follows: 0–2 min, 15–30% B; 2–2.5 min, 30–48% B; 2.5–11 min, 48–82% B; 11–
495 11.5 min, 82–99% B; 11.5–12 min, 99% B; 12–12.1 min, 99–15% B; and 12.1–16 min, hold at
496 15% B for re-equilibration. Mass spectrometry was performed on a Q Exactive Plus Quadrupole-
497 Orbitrap (Thermo Fisher Scientific) equipped with a heated electrospray ionization (HESI) source
498 and operated in negative ion mode. Source settings were: sheath gas, 60 a.u.; auxiliary gas, 25 a.u.;
499 sweep gas, 2 a.u.; spray voltage, 3.0 kV; capillary temperature, 320 °C; S-lens RF level, 50%; and
500 auxiliary gas heater temperature, 370 °C. Parallel reaction monitoring (PRM) was carried out with
501 the following parameters: resolution, 17,500 at m/z 200; AGC target, 2×10^5; maximum injection
502 time, 50 ms; isolation window, m/z 1.2; and stepped normalized collision energies of 20, 30, and
503 40. The oxidized lipid analysis was adapted by previous PRM based analysis[52]. To generate the

504 PRM inclusion list, pooled sample extracts were first analyzed in DDA mode to identify the most
505 abundant polyunsaturated PC and PE species using Lipostar2[53]. These precursors were subjected
506 to in silico oxidation using LPPtiger2 to predict candidate oxidized lipids. A semi-targeted DDA
507 experiment was then conducted to confirm precursor detectability and finalize the inclusion list. [52]
508 Data were analyzed using Skyline (v24.1)[54]. Quantification was based on fragment anions derived
509 from oxidized fatty acyl chains, with peak areas normalized to PC(15:0/18:1(d7)) or
510 PE(15:0/18:1(d7)) internal standards from the EquiSPLASH LIPIDOMIX® mixture.
511
512 *CoQ_9 and CoQ_9H_2 analysis*
513 CoQ_9 and CoQ_9H_2 analysis was conducted by modification of previous study[55]. The D_9-CoQ_{10}
514 standard was purchased from IsoSciences (Ambler, PA, USA). The D_6-$CoQ_{10}H_2$ standard was
515 synthesized from D_6-CoQ_{10}, which was obtained from Good Laboratory Practice Bioscience
516 (Montclair, CA, USA). The CoQ_9 standard was purchased from Tokyo Chemical Industry (Tokyo,
517 Japan), and CoQ_9H_2 was synthesized from CoQ_9. D_6-$CoQ_{10}H_2$ and D_9-CoQ_{10} were used as internal
518 standards for the CoQ_9H_2 and CoQ_9, respectively. Chloroform: methanol (2:1, v/v), containing
519 internal standards of 0.5 μM of D_6-$CoQ_{10}H_2$ and D_6-CoQ_{10} was used to extract mouse lung cancer
520 tissue at a tissue concentration of 25 mg mL^{-1}. For the cells, 1.0×10^7 cells were extracted by one
521 milliliter of same extraction solvent. Samples were then sonicated on ice for 1 min using a VCX
522 130 probe sonicator (5 s on/off cycles), incubated for 30 min, and centrifuged at 17,000 × g for
523 20 min at 4 °C. A 100 μL aliquot of the supernatant was transferred to glass autosampler vials for
524 LC–MS/MS analysis. The liquid chromatography conditions were identical to those used for
525 oxidized lipid analysis. Q Exactive Plus MS was operated in positive ion mode. Source settings
526 were as follows: sheath gas, 60 a.u.; auxiliary gas, 25 a.u.; sweep gas, 2 a.u.; spray voltage, 3.0 kV;

527 capillary temperature, 320 °C; S-lens RF level, 50%; and auxiliary gas heater temperature, 370 °C.
528 The mass range was m/z 120–1,200; resolution, 70,000 at m/z 200; AGC target, 1×10^6; and
529 maximum injection time, 100ms. By using EL–MAVEN (v0.12.0), the LC-MS peaks of CoQ_9,
530 CoQ_9H_2, D_6-$CoQ_{10}H_2$, D_6-CoQ_{10}, and D_9-CoQ_{10} were identified by matching with standard library
531 and their peak areas were extracted with 10 ppm error range. Standard curves were generated using
532 known concentrations of CoQ_9H_2 and CoQ_9, and used to calculate the concentrations of CoQ_9H_2
533 and CoQ_9 in the samples fallowing an algorithm described in a previous study[55].
534
535 *Immunohistochemistry*
536 Tumor bearing mice were euthanized by carbon dioxide asphyxiation, after which the lungs were
537 dissected and fixed in 4% PFA solution overnight. Fixed lungs were washed with PBS 2x,
538 transferred, and stored in 70% ethanol, until cassette loading and paraffin embedding. Sections
539 were cut and stained with H&E. For immunohistochemistry with the exception of TUNEL
540 staining, sections were immunostained on a Leica BondRX automated stainer according to the
541 manufacturer's instructions. In brief, tissues underwent deparaffinization online, followed by
542 epitope retrieval for 20 minutes at 100º with Leica Biosystems ER2 solution (pH9, cat#AR9640),
543 endogenous peroxidase activity blocking with H2O2, and non-specific binding site blocking with
544 Rodent Block M (Biocare, cat# RBM961L) and Bond Primary Antibody Diluent (Leica
545 Biosystems, cat# AR9352). Sections were then incubated with primary antibodies against Gpx4
546 (Abcam), Fsp1 (courtesy of Dr. Marcus Conrad), 4-HNE (JaICA), Ki67, and Ccasp3 for 60
547 minutes at room temperature. Primary antibodies were detected with anti-rat HRP-conjugated
548 polymer (Biocare, cat# BRR4016H), 3,3'-diaminobenzidine (DAB) substrate (provided in the
549 Leica BOND Polymer Refine Detection System, cat# DS9800), and for 4-HNE staining Bond

550 DAB Enhancer (Leica Biosystems, cat# AR9432). Following counter-staining with hematoxylin,
551 slides were scanned at 40X on a Hamamatzu Nanozoomer (2.0HT). TUNEL staining was
552 performed by Histowiz Inc. (histowiz.com) according to their protocol.
553 For OPAL imaging, coronal 5 µm sections were immunostained on a Leica BondRx auto-stainer
554 according to the manufacturer's instructions. In brief, sections were deparaffiinized online and
555 then treated with 3% H_2O_2 to inhibit endogenous peroxidases, followed by antigen retrieval with
556 either ER1 (Leica, AR9961; pH6) or ER2 (Leica, AR9640; pH9) retrieval buffer at 100o for 20
557 minutes. After blocking with either Rodent Block M (Biocare, RBM961L) or Primary Antibody
558 Diluent (Leica, AR93520), slides were incubated with the first primary antibody (FSP1, courtesy
559 of Marcus Conrad, pERK1/2, CST, GPX4, Abcam) and secondary HRP polymer pair, followed
560 by HRP-mediated tyramide signal amplification with a specific Opal® fluorophore. Once the
561 Opal® fluorophore was covalently linked to the antigen, primary and secondary antibodies were
562 removed with a heat retrieval step. This sequence was repeated three more times with subsequent
563 primary and secondary antibody pairs, using a different Opal fluorophore with each primary
564 antibody (see table below for primary antibody sequence and reagent details). After antibody
565 staining, sections were counterstained with spectral DAPI (Akoya Biosciences, FP1490) and
566 mounted with ProLong Gold Antifade (ThermoFisher Scientific, P36935). Semi-automated image
567 acquisition was performed on an Akoya Vectra Polaris (PhenoImagerHT) multispectral imaging
568 system. Slides were scanned at 20X magnification using PhenoImagerHT 2.0 software in
569 conjunction with Phenochart 2.0 and InForm 3.0 to generate unmixed whole slide qptiff scans. All
570 image files were uploaded to the NYUGSoM's OMERO Plus image data management system
571 (Glencoe Software).
572

573 *Flow Cytometry*

574 Lung tissue was processed into a single cell suspension for flow cytometry as previously
575 described[43,56]. Briefly, prior to euthanasia, mice were injected with 2 ug of Anti-mouse CD45-
576 APC conjugated antibody (Biolegend, Clone 30-F11, 103111) retro-orbitally. Lungs were
577 harvested and digested with Collagenase (Sigma-Aldrich, C5138) and deoxyribonuclease I
578 (Sigma-Aldrich, DN25) followed by red blood cell lysis. Single cells were then resuspended in
579 FACS buffer and stained using the following antibodies: CD45 (Biolegend, 103132), CD11b
580 (Biolegend, 101216), CD11c (Biolegend, 117324), Ly6G (Biolegend, 127622), MHCII (BD,
581 748708), CD103 (Biolegend, 121433), CD64 (Biolegend, 139309), SiglecF (BD, 740956),
582 MertK (R&D, BAF591), CD45 (BD, 748371), CD3e (BD, 740854), CD4 (Invitrogen,
583 MCD0428), CD8a (EBioscience, 563152), Secondary (Streptavidin) (BD, 564176). Samples
584 were run on the BD LSRFortessa and analyzed on FlowJo version 10. Gating strategy can be
585 accessed in Supplementary Data 2.

586

587 *TCGA analyses*

588 Gene expression profiles of primary tumors and relevant clinical data of 515 LUAD patients were
589 obtained from The Cancer Genome Atlas6 (TCGute.org). GPX4 and FSP1 (AIFM2) mutational
590 status of TCGA tumor samples was retrieved from cBioPortal151 using the TCGA PanCancer
591 Atlas collection (gdc.cancer.gov/about- data/publications/pancanatlas). For survival data, patients
592 were stratified based on GPX4 or FSP1 expression and overall survival rates were plotted to
593 compare high-GPX4/FSP1 expressing patients (top 50% above median expression) with the rest
594 of the cohort (n=464 patients). All survival analyses were conducted using the survival curve
595 analyses in GraphPad Prism v9.

596

597 *Statistics and Reproducibility*

598 Statistical analysis was performed using GraphPad Prism v9. All data is expressed as mean plus
599 standard error of the mean, unless otherwise specified. Data was analyzed by statistical test
600 indicated in figure legends. All tests were two-tailed and replicates are biological unless otherwise
601 stated. All western blots were replicated at least 3 times with results reproducible of data shown in
602 figures. All *in vitro* assays were replicated at least 3 times with a minimum of n=3 biological
603 replicates per group for statistical power. For all *in vivo* experiments, the minimum sample size
604 was 4 independent mice/tumors and respective sample size per genotype/condition is further
605 specified in the figure legend. Sample size was not calculated but was chosen in each experiment
606 based on previous experience with various models and to ensure that there were enough samples
607 for statistical power. All *in vivo* experiments were replicated at least twice with results reproducible
608 of data shown in figures. When representative images are shown, a minimum of 3 samples from
609 the larger cohort were stained from each group. In the case of representative MRI images, all
610 animals from the cohort were imaged. During sample processing and analysis for the lipidomic
611 the samples were given numeric IDs which after analysis, were unblinded and graphed. For
612 histological and immunohistochemistry analysis, researcher was blinded to the sample condition.
613 The investigators were not blinded during most other data collection or analysis. Biorender[57] was
614 used to make the schematics and diagrams.

615

Methods References

51 Winslow, M.M., *et al.* Suppression of lung adenocarcinoma progression by Nkx2-1. *Nature* **473**, 101-104 (2011).

52. Criscuolo, A., *et al.* Analytical and computational workflow for in-depth analysis of oxidized complex lipids in blood plasma. *Nature Communications* **13**, 6547 (2022).

53. Goracci, L., *et al.* Lipostar, a Comprehensive Platform-Neutral Cheminformatics Tool for Lipidomics. *Analytical Chemistry* **89**, 6257-6264 (2017).

54. Adams, K.J., *et al.* Skyline for Small Molecules: A Unifying Software Package for Quantitative Metabolomics. *Journal of Proteome Research* **19**, 1447-1458 (2020).

55. Kang, Y.P., Kim, T.H., Ngoc Nguyen, C.T., Kim, S.M. & Kwon, S.W. Robust Determination of Coenzyme Q10 Redox Status Using Two Isotope-Labeled Internal Standards. *Available at SSRN 4982487*.

56. Pillai, R., *et al.* Glutamine antagonist DRP-104 suppresses tumor growth and enhances response to checkpoint blockade in KEAP1 mutant lung cancer. *Sci Adv* **10**, eadm9859 (2024).

57. Created in BioRender. Vaughan, A. (2025) https://BioRender.com/99qhixq

Data Availability

All data and raw gel images are included with the paper. Raw lipidomic data have been deposited in the MassIVE data base (https://massive.ucsd.edu/) under accession number MSV000098883. Analyzed lipidomic data are available in Supplementary Data 3. Gene expression profiles of primary tumors and relevant clinical data of 515 LUAD patients were obtained from The Cancer Genome Atlas6 (TCGute.org). GPX4, FSP1 (AIFM2), KRAS, EGFR, KEAP1, and STK11 mutational status of TCGA tumor samples was retrieved from cBioPortal151 using the TCGA PanCancer Atlas collection (gdc.cancer.gov/about- data/publications/pancanatlas). All other materials are available upon request from the corresponding author (T.P.). Source data are provided with this paper.

Acknowledgements

We dedicate this work to Judy Teixeira, whose love, strength, and spirit continue to inspire us. We thank Gyles Ward and Cynthia Loomis from the Experimental Pathology Core [RRID:SCR_017928] at NYU Langone Health, which is partially supported by the Cancer Center Support Grant P30CA016087 at NYU Langone's Laura and Isaac Perlmutter Cancer Center, for support with IHC staining and imaging. The PhenoImagerHT Mutlispectral imaging system was initially purchased through a Shared Instrumentation Grant S10OD021747. We thank the Wayne State University School of Medicine Lipidomics Core Facility, which is supported in part by National Center for Research Resources, National Institutes of Health Grants S10RR027926 and S10OD032292, for support with LC-MS. We also recognize that the analysis of Fsp1 oxidized lipids and CoQ_9 were conducted by the Proteomics and Metabolomics Core at the College of Pharmacy, Seoul National University, South Korea. We thank R. Possemato and S. Kotschi for critical reading of this manuscript. T. P. is supported by NIH grants (R37CA222504, R01CA227649, R01CA283049, R01CA262562) and an American Cancer Society Research Scholar Grant (RSG-17-20001–TBE). K.W. is supported by the Ruth L. Kirschstein Individual Predoctoral NRSA fellowship (F30CA275258) and NIH training grants (T32GM136573, T32GM136542). A.J.V. is supported by the NIH training grant (T32GM136542). M.C. received funding from the Deutsche Forschungsgemeinschaft (DFG) (CO 291/7-1, the Priority Program SPP 2306 [CO 291/9-1, #461385412; CO 291/10-1, #461507177] and the European Research Council (ERC) under the European Union's Horizon 2020 research and innovation program (grant agreement No. GA 884754).

670 **Author contributions**

671 T.P., K.W., A.J.V. designed and directed the study. K.W., A.J.V., J.P.B., A.Z., M.N.N., M.M., and
672 S.C. performed various *in vitro* and *in vivo* experiments reported in the study. R.P. performed
673 FACS. Y.H. performed TCGA patient data analyses. S.M.K. performed Fsp1 epilipidomics and
674 COQ measurement, T.H.K assisted with data analysis, and was supervised by Y.P.K. S.C.
675 performed unbiased tumor burden quantification. S.R. maintained and genotyped all experimental
676 mice. M.C., T.N., D.S., M.H., provided conceptual advice. T.P., K.W., and A.J.V. wrote the
677 manuscript with comments and input from all authors.

678

679 **Competing Interests**

680 T.P. received funding from Pfizer Medical Education Group, Dracen Pharmaceuticals, Kymera
681 Therapeutics, Bristol Myers Squibb, and Agios Pharmaceuticals not related to the submitted work.
682 M.C. is a co-founder and shareholder of ROSCUE Therapeutics GmbH. M.C. and T.N. have filed
683 a patent (WO2024115673A1) for some of the FSP1 inhibitor compounds described herein. All
684 other authors declare no competing interests.

685 **REFERENCES**

686 1. Dixon, S.J., *et al.* Ferroptosis: an iron-dependent form of nonapoptotic cell death. *Cell* **149**,
687 1060-1072 (2012).
688 2. Viswanathan, V.S., *et al.* Dependency of a therapy-resistant state of cancer cells on a lipid
689 peroxidase pathway. *Nature* **547**, 453-457 (2017).
690 3. Hangauer, M.J., *et al.* Drug-tolerant persister cancer cells are vulnerable to GPX4
691 inhibition. *Nature* **551**, 247-250 (2017).
692 4. Berndt, C., *et al.* Ferroptosis in health and disease. *Redox Biol* **75**, 103211 (2024).
693 5. Nakamura, T. & Conrad, M. Exploiting ferroptosis vulnerabilities in cancer. *Nat Cell Biol*
694 (2024).
695 6. Friedmann Angeli, J.P., *et al.* Inactivation of the ferroptosis regulator Gpx4 triggers acute
696 renal failure in mice. *Nat Cell Biol* **16**, 1180-1191 (2014).
697 7. Yang, W.S., *et al.* Regulation of ferroptotic cancer cell death by GPX4. *Cell* **156**, 317-331
698 (2014).
699 8. Bersuker, K., *et al.* The CoQ oxidoreductase FSP1 acts parallel to GPX4 to inhibit
700 ferroptosis. *Nature* **575**, 688-692 (2019).
701 9. Doll, S., *et al.* FSP1 is a glutathione-independent ferroptosis suppressor. *Nature* **575**, 693-
702 698 (2019).
703 10. Wiernicki, B., *et al.* Excessive phospholipid peroxidation distinguishes ferroptosis from
704 other cell death modes including pyroptosis. *Cell Death Dis* **11**, 922 (2020).
705 11. Conrad, M. & Pratt, D.A. The chemical basis of ferroptosis. *Nat Chem Biol* **15**, 1137-1147
706 (2019).
707 12. Dixon, S.J. & Olzmann, J.A. The cell biology of ferroptosis. *Nat Rev Mol Cell Biol* **25**,
708 424-442 (2024).
709 13. Kraft, V.A.N., *et al.* GTP Cyclohydrolase 1/Tetrahydrobiopterin Counteract Ferroptosis
710 through Lipid Remodeling. *ACS Cent Sci* **6**, 41-53 (2020).
711 14. Soula, M., *et al.* Metabolic determinants of cancer cell sensitivity to canonical ferroptosis
712 inducers. *Nat Chem Biol* **16**, 1351-1360 (2020).
713 15. Garcia-Bermudez, J., *et al.* Squalene accumulation in cholesterol auxotrophic lymphomas
714 prevents oxidative cell death. *Nature* **567**, 118-122 (2019).
715 16. Qiu, B., *et al.* Phospholipids with two polyunsaturated fatty acyl tails promote ferroptosis.
716 *Cell* **187**, 1177-1190 e1118 (2024).
717 17. Kagan, V.E., *et al.* Oxidized arachidonic and adrenic PEs navigate cells to ferroptosis. *Nat*
718 *Chem Biol* **13**, 81-90 (2017).
719 18. Doll, S., *et al.* ACSL4 dictates ferroptosis sensitivity by shaping cellular lipid composition.
720 *Nat Chem Biol* **13**, 91-98 (2017).
721 19. Dixon, S.J., *et al.* Human Haploid Cell Genetics Reveals Roles for Lipid Metabolism
722 Genes in Nonapoptotic Cell Death. *ACS Chem Biol* **10**, 1604-1609 (2015).
723 20. Mishima, E., *et al.* A non-canonical vitamin K cycle is a potent ferroptosis suppressor.
724 *Nature* **608**, 778-783 (2022).
725 21. Seiler, A., *et al.* Glutathione peroxidase 4 senses and translates oxidative stress into 12/15-
726 lipoxygenase dependent- and AIF-mediated cell death. *Cell Metab* **8**, 237-248 (2008).
727 22. Zilka, O., *et al.* On the Mechanism of Cytoprotection by Ferrostatin-1 and Liproxstatin-1
728 and the Role of Lipid Peroxidation in Ferroptotic Cell Death. *ACS Cent Sci* **3**, 232-243
729 (2017).

730 23. Jiang, X., Stockwell, B.R. & Conrad, M. Ferroptosis: mechanisms, biology and role in
731 disease. *Nat Rev Mol Cell Biol* **22**, 266-282 (2021).
732 24. Nakamura, T.*, et al.* Phase separation of FSP1 promotes ferroptosis. *Nature* **619**, 371-377
733 (2023).
734 25. Eaton, J.K.*, et al.* Selective covalent targeting of GPX4 using masked nitrile-oxide
735 electrophiles. *Nat Chem Biol* **16**, 497-506 (2020).
736 26. Yang, W.S. & Stockwell, B.R. Synthetic lethal screening identifies compounds activating
737 iron-dependent, nonapoptotic cell death in oncogenic-RAS-harboring cancer cells. *Chem*
738 *Biol* **15**, 234-245 (2008).
739 27. Xavier da Silva, T.N., Schulte, C., Alves, A.N., Maric, H.M. & Friedmann Angeli, J.P.
740 Molecular characterization of AIFM2/FSP1 inhibition by iFSP1-like molecules. *Cell*
741 *Death Dis* **14**, 281 (2023).
742 28. Hendricks, J.M.*, et al.* Identification of structurally diverse FSP1 inhibitors that sensitize
743 cancer cells to ferroptosis. *Cell Chem Biol* **30**, 1090-1103 e1097 (2023).
744 29. Nakamura, T.*, et al.* Integrated chemical and genetic screens unveil FSP1 mechanisms of
745 ferroptosis regulation. *Nat Struct Mol Biol* **30**, 1806-1815 (2023).
746 30. Yoshioka, H.*, et al.* Identification of a Small Molecule That Enhances Ferroptosis via
747 Inhibition of Ferroptosis Suppressor Protein 1 (FSP1). *ACS Chem Biol* **17**, 483-491 (2022).
748 31. Sanchez-Rivera, F.J.*, et al.* Rapid modelling of cooperating genetic events in cancer
749 through somatic genome editing. *Nature* **516**, 428-431 (2014).
750 32. Ding, H.*, et al.* Activation of the NRF2 antioxidant program sensitizes tumors to G6PD
751 inhibition. *Sci Adv* **7**, eabk1023 (2021).
752 33. Lignitto, L.*, et al.* Nrf2 Activation Promotes Lung Cancer Metastasis by Inhibiting the
753 Degradation of Bach1. *Cell* **178**, 316-329.e318 (2019).
754 34. Romero, R.*, et al.* Keap1 loss promotes Kras-driven lung cancer and results in dependence
755 on glutaminolysis. *Nat Med* **23**, 1362-1368 (2017).
756 35. Best, S.A.*, et al.* Distinct initiating events underpin the immune and metabolic
757 heterogeneity of KRAS-mutant lung adenocarcinoma. *Nat Commun* **10**, 4190 (2019).
758 36. Takahashi, N.*, et al.* 3D Culture Models with CRISPR Screens Reveal Hyperactive NRF2
759 as a Prerequisite for Spheroid Formation via Regulation of Proliferation and Ferroptosis.
760 *Mol Cell* **80**, 828-844 e826 (2020).
761 37. Zou, Y.*, et al.* A GPX4-dependent cancer cell state underlies the clear-cell morphology and
762 confers sensitivity to ferroptosis. *Nat Commun* **10**, 1617 (2019).
763 38. Vidigal, J.A. & Ventura, A. Rapid and efficient one-step generation of paired gRNA
764 CRISPR-Cas9 libraries. *Nat Commun* **6**, 8083 (2015).
765 39. Ingold, I.*, et al.* Selenium Utilization by GPX4 Is Required to Prevent Hydroperoxide-
766 Induced Ferroptosis. *Cell* **172**, 409-422 e421 (2018).
767 40. Cancer Genome Atlas Research, N. Comprehensive molecular profiling of lung
768 adenocarcinoma. *Nature* **511**, 543-550 (2014).
769 41. Muller, F.*, et al.* Elevated FSP1 protects KRAS-mutated cells from ferroptosis during
770 tumor initiation. *Cell Death Differ* **30**, 442-456 (2023).
771 42. Koppula, P.*, et al.* A targetable CoQ-FSP1 axis drives ferroptosis- and radiation-resistance
772 in KEAP1 inactive lung cancers. *Nat Commun* **13**, 2206 (2022).
773 43. Zavitsanou, A.M.*, et al.* KEAP1 mutation in lung adenocarcinoma promotes immune
774 evasion and immunotherapy resistance. *Cell Rep* **42**, 113295 (2023).

775 44. Wu, K., El Zowalaty, A.E., Sayin, V.I. & Papagiannakopoulos, T. The pleiotropic
776 functions of reactive oxygen species in cancer. *Nat Cancer* **5**, 384-399 (2024).
777 45. Cheung, E.C. & Vousden, K.H. The role of ROS in tumour development and progression.
778 *Nat Rev Cancer* **22**, 280-297 (2022).
779 46. Yant, L.J.*, et al.* The selenoprotein GPX4 is essential for mouse development and protects
780 from radiation and oxidative damage insults. *Free Radic Biol Med* **34**, 496-502 (2003).
781 47. Mei, J., Webb, S., Zhang, B. & Shu, H.B. The p53-inducible apoptotic protein AMID is
782 not required for normal development and tumor suppression. *Oncogene* **25**, 849-856
783 (2006).
784 48. Nguyen, H.P.*, et al.* Aifm2, a NADH Oxidase, Supports Robust Glycolysis and Is Required
785 for Cold- and Diet-Induced Thermogenesis. *Mol Cell* **77**, 600-617 e604 (2020).
786 49. Drijvers, J.M.*, et al.* Pharmacologic Screening Identifies Metabolic Vulnerabilities of
787 CD8(+) T Cells. *Cancer Immunol Res* **9**, 184-199 (2021).
788 50. Matsushita, M.*, et al.* T cell lipid peroxidation induces ferroptosis and prevents immunity
789 to infection. *J Exp Med* **212**, 555-568 (2015).
790

791 **Main Figure Legends**

792 **Fig. 1: Gpx4 loss triggers ferroptosis in lung tumors**

793 **(a)** Schematic of KP LUAD GEMMs intratracheally infected with pUSEC lentiviruses containing
794 dual sgRNAs targeting Neo (control; n=13) or Gpx4 (n=13). Mice were dosed with Liproxstatin-
795 1 (LIP1; sg*Neo* n=6, sg*Gpx4* n=7) or Vehicle (Veh; sg*Neo* n=6, sg*Gpx4* n=7) every other day
796 starting from tumor initiation to experiment endpoint. **(b)** Tumor burden of KP LUAD tumors with
797 control (sg*Neo*) or Gpx4 (sg*Gpx4*) knockout, treated with either Veh or LIP1. **(c)** Representative
798 MRI of KP LUAD tumors with control (sg*Neo*) or Gpx4 (sg*Gpx4*) knockout, treated with either
799 Veh or LIP1. **(d)** Representative H&E of KP LUAD tumors with control (sg*Neo*) or Gpx4
800 (sg*Gpx4*) knockout, treated with either Veh or LIP1. Scale bars: 2000µm. **(e)** Tumor 4-HNE
801 expression by IHC of KP LUAD tumors with control (sg*Neo*) or Gpx4 (sg*Gpx4*) knockout, treated
802 with either Veh or LIP1. **(f)** Representative 4-HNE IHC staining from (e). Scale bars: 20µm. Data
803 are represented as mean values, error bars represent SEM, significance determined via one-way
804 ANOVA with multiple comparisons (panels b, e).

805

806 **Fig. 2: Fsp1 knockout robustly restricts lung tumorigenesis**

807 **(a)** Schematic depicting mechanisms of Fsp1- and Gpx4-mediated buffering against cellular lipid
808 peroxidation and ferroptosis. **(b)** Overall survival of *KRAS*-mutant LUAD patients (n=280) from
809 TCGA, stratified by high versus low primary tumor *FSP1* (*AIFM2*) expression. Median survival
810 for FSP1 high versus low was 1215 days and 1498 days, respectively (hazard ratio 1.51 [1.01-
811 2.25]). **(c)** Representative IHC for Fsp1 and Gpx4 in KP LUAD GEMM adenomas versus
812 adenocarcinomas. Scale bars: 100µm. **(d)** Tumor Fsp1 expression by IHC of KP LUAD GEMM
813 tumors at 10- versus 14-weeks post tumor initiation. **(e)** Schematic of KP LUAD GEMMs

814 intratracheally infected with pUSEC lentiviruses containing double sgRNAs targeting control
815 (Neo; n=4), Fsp1 (n=6), or Gpx4 (n=6). **(f)** Tumor burden of KP LUAD tumors with knockout of
816 either control (Neo), Fsp1, or Gpx4. **(g)** Representative H&E of KP LUAD tumors with knockout
817 of either control (Neo), Fsp1, or Gpx4. Scale bars: 2000µm. **(h)** Relative proportion of KP
818 adenomas versus adenocarcinomas with knockout of either control (Neo), Fsp1, or Gpx4. **(i)**
819 Representative TUNEL staining of KP, $Fsp1^{KO}$ and $Fsp1^{WT}$ orthotopic lung tumors. Scale bars:
820 50µm **(j)** Schematic depicting generation of isogenic Fsp1-wildtype ($Fsp1^{WT}$) versus Fsp1-
821 knockout ($Fsp1^{KO}$) cells for paralleled *in vitro* assays and *in vivo* syngeneic orthotopic
822 transplantation studies. **(k)** Representative images of crystal violet clonogenic growth assay in
823 isogenic KP, $Fsp1^{KO}$ and $Fsp1^{WT}$ cells treated with RSL3 (0.5µM) ± LIP1 (100nM). **(l)** Tumor
824 burden of KP, $Fsp1^{KO}$ (n=8) and $Fsp1^{WT}$ (n=7) orthotopic lung tumors. **(m)** Representative H&E
825 of KP, $Fsp1^{KO}$ and $Fsp1^{WT}$ orthotopic lung tumors. Scale bars: 2000µm. Data are represented as
826 mean values, error bars represent SEM, significance determined via two-sided student's t-test
827 (panels d and l), one-way ANOVA with multiple comparisons (panel f) or Kaplan-Meier simple
828 survival analysis (panel b).
829
830 **Fig. 3: Sensitivity to FSP1 loss is not dependent on tumor mutations or lineage**
831 Longitudinal tumor growth and endpoint tumor weights from indicated cell lines with
832 CRISPR/Cas9-mediated knockout of FSP1 (sg*FSP1*) or control (sg*TOM*, sg*Neo*), transplanted as
833 subcutaneous (subQ) xenograft tumors into NSG mice: **(a)** H2009, sg*FSP1* (n=8) or control (n=8).
834 **(b)** H1299, sg*FSP1* (n=9) or control (n=9). **(c)** PC9, sg*FSP1* (n=9) or control (n=9). **(d)** H1975,
835 sg*FSP1* (n=8) or control (n=9). **(e)** A549, sg*FSP1* (n=9) or control (n=10). **(f)** 16645, sg*Fsp1*(n=7)
836 or control (n=9). **(g)** KPC7 (murine PDAC), sg*Fsp1* (n=9) or control (n=10). Data are represented

837 as mean values, error bars represent SEM, significance determined via two-sided student's t test
838 (panels a-g)
839
840 **Fig. 4: FSP1 is required for the suppression of ferroptosis *in vivo***
841 **(a)** Heatmap of indicated oxidized PE/PC lipid species detected via LC/MS from KP, $Fsp1^{KO}$ and
842 $Fsp1^{WT}$ orthotopic lung tumors. **(b)** Longitudinal growth of KP, $Gpx4^{KO}$ subQ xenograft tumors
843 with $Fsp1^{OE}$ (n=10) versus control ($empty^{OE}$, n=9) in C57BL/6J mice. **(c)** Longitudinal growth of
844 KP, $Fsp1^{KO}$ subQ xenograft tumors with either Fsp1 restoration ($Fsp1^{WT}$, n=9), Gpx4
845 overexpression ($Gpx4^{OE}$, n=8), or controls ($empty^{OE}$, n=9; $Fsp1^{KO}$ n=8) in C57BL/6J mice. **(d)**
846 Ratio of CoQ_9H_2/CoQ_9 detected via LC/MS in KP, $Fsp1^{KO}$ and $Fsp1^{WT}$ orthotopic lung tumors
847 versus cells treated with DMSO or RSL3 (0.5 μM) for 8 hours. **(e)** Schematic depicting Acsl4's
848 pro-ferroptotic function. **(f)** Tumor burden in C57BL/6J mice with KP, $Fsp1^{KO}$ and $Fsp1^{WT}$
849 orthotopic lung tumors with CRISPR/Cas9-mediated Acsl4 or control (Neo) deletion (WT n=5,
850 $Acsl4^{KO}$ n=4, $Fsp1^{KO}$ n=7, $Fsp1^{KO}Acsl4^{KO}$ n=7). **(g)** Schematic depicting dietary Vitamin E (VitE)
851 manipulation studies in (h) and (i). **(h)** Longitudinal lung tumor growth (measured via
852 bioluminescence normalized to first timepoint) in C57BL/6J mice orthotopically transplanted with
853 KP, $Fsp1^{KO}$ cells and receiving high (n=8) or low (n=7) VitE diets *ad libitum* 5 days pre-tumor
854 initiation. **(i)** Longitudinal lung tumor growth (measured via bioluminescence) in C57BL/6J mice
855 orthotopically transplanted with KP, $Fsp1^{KO}$ cells and placed on high (n=6) or low (n=6) VitE diets
856 *ad libitum* after tumor establishment (day18). **(j)** Schematic of KP LUAD GEMMs intratracheally
857 infected with pUSEC lentiviruses containing double sgRNAs targeting Neo (control, n=12) or
858 Fsp1 (n=12). Mice were dosed with Liproxstatin-1 (LIP1, n=6 per genotype) or Vehicle (Veh, n=6
859 per genotype) daily starting 5 weeks post-tumor initiation. **(k)** Tumor burden of experiment in (j).

860 **(l)** Representative H&E of tumors of experiment in (j). Scale bars: 100µm. Data are represented
861 as mean values, error bars represent SEM, significance determined via two-sided student's t test
862 (panel b, d, f, h, i, k) or two-way ANOVA with Tukey's multiple comparison test (panel c).
863
864 **Fig. 5: FSP1 is a viable therapeutic target for *KRAS*-mutant lung adenocarcinoma**
865 **(a)** Overall survival of C57BL/6J mice with orthotopic lung tumors with $Fsp1^{KO}$ (n=7) or hFSP1
866 re-expression, treated with either icFSP1 (n=8) or Vehicle (n=7). **(b)** Longitudinal lung tumor
867 growth (measured via bioluminescence) in C57BL/6J mice orthotopically transplanted with
868 $hFSP1^{WT}$ cells and treated with either Vehicle (n=8), LIP1 (n=7), icFSP1 (n=8), or icFSP1+LIP1
869 (n=8). **(c)** Overall survival of C57BL/6J mice with $Fsp1^{KO}$ (n=5), $hFSP1^{WT}$, or $hFSP1^{Q319K}$-
870 expressing tumors, treated with icFSP1 ($hFSP1^{WT}$, n=5; $hFSP1^{Q319K}$, n=7) or Vehicle ($hFSP1^{WT}$,
871 n=7; $hFSP1^{Q319K}$, n=7). **(d)** Longitudinal growth of PDX LX465 tumors treated with icFSP1
872 (n=10) or Vehicle (n=10) in NSG mice. Data are represented as mean values, error bars represent
873 SEM, significance determined via two-way ANOVA with Tukey's multiple comparisons test
874 (panel b), two-sided student's t-test (panel d), or Kaplan-Meier simple survival analysis (panels a,
875 c).
876
877
878
879
880
881
882

883 **Extended Data Figure Legends**

884 **Extended Data Fig. 1: Gpx4 is required by lung cancer cells**

885 **(a)** Quantification and representative images of Gpx4 IHC in KP LUAD GEMM tumors with
886 knockout of either control (Neo, n=11) or Gpx4 (n=12). Scale bars: 200µm. **(b)** Representative 4-
887 hydroxy-2-noneal (4-HNE) IHC of liver tissue from conditional *Gpx4*-knockout mice. Scale bars:
888 100µm. **(c)** Top: Western blot of KP LUAD cells with CRISPR/Cas9-mediated genetic deletion
889 of Gpx4 with either two individual or duplexed sgRNAs. Bottom: Representative images of crystal
890 violet clonogenic assay of KP LUAD cells with knockout of either control (Neo) or Gpx4. Cells
891 were treated with 100nM LIP1. **(d)** Heatmap of LC-MS detection of oxidized phospholipids in KP
892 LUAD cells treated with DMSO control, RSL3 (0.5µM), and RSL3 (0.5µM) + LIP1 (100nM) for
893 8 hours. **(e)** Schematic of Gpx4 ectopic overexpression (OE) method in KP LUAD cells. Western
894 blot and representative images of crystal violet clonogenic assay of KP LUAD cells with wildtype
895 (WT) or OE of Gpx4. **(f)** CellTiter-Glo Luminescence viability assay of KP, $Gpx4^{WT}$ or $Gpx4^{OE}$
896 cells upon increasing concentrations of RSL3 (n=5 per group). **(g)** Western blot of KP LUAD cells
897 treated with 20nM Na_2SeO_3 or DMSO. CellTiter-Glo Luminescence viability assay of KP LUAD
898 cells treated with 20nM Na_2SeO_3 or DMSO with increasing RSL3 addition (n=5 per group). **(h)**
899 *GPX4* expression in *KRAS*-mutant primary LUAD tumors from TCGA, divided into early and late
900 tumor stages (normal lung, n=54; stage I/II, n=354; stage III/IV, n=98). **(i)** Overall survival of
901 *KRAS*-mutant LUAD patients (n=464) from TCGA, stratified by high vs low tumor *GPX4*
902 expression. **(j)** Tumor Gpx4 IHC quantification of KP LUAD GEMM tumors at 10 weeks (n=4)
903 vs 14 weeks (n=4) post-tumor initiation. Box plots indicate median (middle line), 25th, 75th
904 percentile (box) and 5th and 95th percentile (whiskers). Data are represented as mean values, error
905 bars represent SEM, significance determined via one-way ANOVA with multiple comparisons

906 (panel h), two-sided student's t-test (panel j) or Kaplan-Meier simple survival analysis (panel i).
907 For gel source data, see Supplementary Data 1.
908
909 **Extended Data Fig. 2: FSP1's anti-ferroptotic function is not dependent on oncogenic**
910 **signaling**
911 **(a)** *FSP1* (*AIFM2*) expression of *KRAS*-mutant primary LUAD tumors from TCGA, divided into
912 early and late tumor stages (normal lung, n=54; stage I/II, n=354; III/IV, n=98). **(b)** *FSP1* (*AIFM2*)
913 expression of *KRAS*-mutant primary LUAD tumors from TCGA, separated by the *KRAS* mutation
914 (G12C n=51; G12V n=32; G12D n=17; G12A n=16; other n=20). **(c)** *FSP1* (*AIFM2*) expression
915 of primary LUAD tumors from TCGA, separated by oncogenic driver mutation (normal lung,
916 n=59; EGFR, n=71; KRAS, n=135; other n=307). **(d)** Western blot of KP LUAD human cell lines
917 treated with 50nM RMC-042 for indicated durations. **(e)** Representative multi-IF images of KP
918 tumors for markers indicated. Panels are 10X, scale bars: 50µm; insets are 20X, scale bars: 20µm.
919 **(f)** *FSP1* (*AIFM2*) expression of *KRAS*-mutant primary LUAD tumors from TCGA, separated by
920 tumor co-mutation status (*KEAP1*/*STK11* WT n=88; *STK11* mutant n=20; *KEAP1* mutant n=16;
921 *KEAP1/STK11* mutant n=11). **(g)** *FSP1* (*AIFM2*) expression in KP LUAD human cell lines treated
922 with an Nrf2 activator, KI696, for 5 days (n=3 per group). Box plots indicate median (middle line),
923 25th, 75th percentile (box) and 5th and 95th percentile (whiskers). Data are represented as mean
924 values, error bars represent SEM, significance determined via one-way ANOVA with multiple
925 comparisons (panels a, b, c, f, g). For gel source data, see Supplementary Data 1.
926
927 **Extended Data Fig. 3: Neither Fsp1 nor Gpx4 have an impact on tumor initiation,**
928 **proliferation, or apoptosis**

929 **(a)** Quantification and representative images of tumor Fsp1 IHC in KP LUAD GEMMs with
930 knockout of either control (Neo, n=11) or Fsp1 (n=14). Scale bars: 100µm. **(b)** Tumor number
931 quantification in KP LUAD GEMMs with tumor-specific knockout of either control (Neo, n=4),
932 Fsp1 (n=7), or Gpx4 (n=6). **(c)** Individual area of KP LUAD GEMM tumors with knockout of
933 either control (Neo, n=465), Fsp1 (n=453), or Gpx4 (n=384). **(d)** Quantification of Ki67 IHC of
934 KP LUAD GEMM tumors with knockout of either control (Neo, n=355), Fsp1 (n=268), or Gpx4
935 (n=291). **(e)** Quantification of cleaved caspase-3 IHC of KP LUAD GEMM tumors with knockout
936 of either control (Neo, n=46), Fsp1 (n=22), or Gpx4 (n=52). Data are represented as mean values,
937 error bars represent SEM, significance determined via one-way ANOVA with multiple
938 comparisons (panels b-e).
939
940 **Extended Data Fig. 4: Fsp1 is required for cell-autonomous tumor growth *in vivo***
941 **(a)** Top: Western blot of KP LUAD cells with CRISPR/Cas9-mediated genetic deletion of Fsp1
942 with either two individual or duplexed sgRNAs. Bottom: Representative images of crystal violet
943 clonogenic assay of KP LUAD cells with knockout of either control (Neo) or Fsp1. Cells were
944 treated with 100nM LIP1. **(b)** Schematic depicting all transplantation models performed using
945 isogenic KP, $Fsp1^{KO}$ and $Fsp1^{WT}$. **(c, d)** Longitudinal growth and endpoint tumor weights of KP
946 sg*Fsp1* (n=8) versus control (sg*Neo* n=10) subcutaneous (subQ) xenograft tumor transplanted into
947 C57BL/6J male mice. **(e)** Longitudinal lung tumor growth (measured via bioluminescence) in
948 C57BL/6J male mice orthotopically transplanted with KP LUAD cells with CRISPR/Cas9-
949 mediated knockout of Fsp1 (n=8) or control (n=7). **(f)** Longitudinal lung tumor growth (measured
950 via bioluminescence normalized to first timepoint (day 7)) in C57BL/6J male mice orthotopically
951 transplanted with isogenic KP, $Fsp1^{KO}$ (n=6) and $Fsp1^{WT}$ (n=7) cells. **(g)** Longitudinal lung tumor

952 growth (measured via absolute bioluminescence) in NU/J immunocompromised mice
953 orthotopically transplanted with isogenic KP, $Fsp1^{KO}$ (n=6) and $Fsp1^{WT}$ (n=7) cells. **(h)**
954 Longitudinal lung tumor growth (measured via absolute bioluminescence) in C57BL/6J female
955 mice with orthotopic transplantation of isogenic KP, $Fsp1^{KO}$ (n=8) and $Fsp1^{WT}$ (n=8) cells. **(i)**
956 Longitudinal tumor growth and endpoint tumor weights of either isogenic KP, $Fsp1^{KO}$ or $Fsp1^{WT}$
957 subcutaneous (subQ) xenograft tumors transplanted in either C57BL/6J WT ($Fsp1^{KO}$, male n=10
958 female n=10; $Fsp1^{WT}$, male n=8, female n=10) or C57BL/6J *Fsp1*-knockout mice ($Fsp1^{KO}$, males
959 n=12, females n=12; $Fsp1^{WT}$, male n=10, female n=10). **(j)** Western blot of KP LUAD cells with
960 wildtype (WT) or overexpression (OE) of Fsp1. Representative images of crystal violet clonogenic
961 assay of KP LUAD cells with $Fsp1^{WT}$ or $Fsp1^{OE}$. **(k)** CellTiter-Glo Luminescence viability assay
962 of KP, $Fsp1^{WT}$ or $Fsp1^{OE}$ cells (5 biological replicates per group) with increasing concentrations
963 of RSL3. **(l, m)** Longitudinal growth and endpoint weights of KP $Fsp1^{WT}$ (n=10) or $Fsp1^{OE}$ (n=10)
964 subcutaneous (subQ) xenograft tumor transplanted into C57BL/6J male mice. Data are represented
965 as mean values, error bars represent SEM, significance determined via one-way ANOVA with
966 multiple comparisons (panel i), two-way ANOVA with Tukey's multiple comparisons test (panels
967 c, e, f, g, h, l), or two-sided student's t-test (panels d, m). For gel source data, see Supplementary
968 Data 1.
969

970 **Extended Data Fig. 5: FSP1 loss *in vitro* does not induce ferroptosis without RSL3**

971 **(a)** Top: Western blot; Bottom: baseline growth (normalized to control); and Right: CellTiter-Glo
972 Luminescence viability assay of H2009 cells with the lentiviral addition of Cas9 and guide RNAs
973 targeting FSP1 or a non-targeting control (TOM) (at least 4 biological replicates per group).
974 Viability assay is upon increasing concentrations of RSL3. **(b)** As in (a), but with H1299 cells. **(c)**

975 As in (a), but with PC9 cells. **(d)** As in (a), but with H1975 cells. **(e)** As in (a), but with A549 cells.
976 **(f)** As in (a), but with 16645 cells. **(g)** As in (a), but with KPC7 cells. Data are represented as mean
977 values, error bars represent SEM, significance determined via two-sided student's t-test (panels a-
978 g). For gel source data, see Supplementary Data 1.
979
980 **Extended Data Fig. 6: Fsp1 loss promotes tumor cell ferroptosis**
981 **(a)** Western blot of KP, Gpx4^{KO} LUAD cells with either empty vector (—) or Fsp1^{OE}. **(b)** Western
982 blot of KP, Fsp1^{KO} LUAD cells with re-expression of either empty vector (—), Fsp1^{WT}, Gpx4^{OE}.
983 **(c)** CellTiter-Glo Luminescence viability assay of KP, Fsp1^{KO} LUAD cells in (b) upon increasing
984 concentrations of RSL3. **(d)** Endpoint tumor weights of subcutaneous (subQ) xenograft tumors
985 from indicated cell lines transplanted in C57BL/6J female mice (control n=10; Fsp1^{WT}, n=9;
986 Gpx4^{OE}; n=8). **(e)** Top: Western blot of KP, Fsp1^{KO} LUAD cells with re-expression of either
987 empty vector (—), wildtype (WT) Fsp1, or mutant (mut) Fsp1. Bottom: Representative images of
988 crystal violet clonogenic assay. **(f)** CellTiter-Glo Luminescence viability assay of KP, Fsp1^{KO}
989 LUAD cells with re-expression of either empty vector (Fsp1^{KO}), Fsp1^{WT}, or Fsp1^{mut} upon
990 increasing concentrations of RSL3. LIP1 used at 100nM. **(g)** Longitudinal tumor growth
991 (measured via bioluminescence normalized to initial imaging timepoint (day14)) in C57BL/6J
992 male mice orthotopically transplanted with isogenic KP, Fsp1^{KO} LUAD cells with re-expression
993 of either empty control vector (Fsp1^{KO}, n=7), Fsp1^{WT} (n=7), or Fsp1^{mut} (n=7). **(h)** Representative
994 images of crystal violet clonogenic assay of KP, Fsp1^{WT} or Fsp1^{KO} LUAD cells with
995 CRISPR/Cas9- mediated knockout of control (Neo) or Acsl4. **(i)** Longitudinal tumor growth
996 (measured by bioluminescence) of C57BL/6J male mice with orthotopic transplantation of
997 isogenic KP, Fsp1^{KO} and Fsp1^{WT} cells with CRISPR/Cas9-mediated knockout of control (Neo) or

998 Acsl4 (WT, n=5; Acsl4^{KO}, n=4; Fsp1^{KO}, n=7; Fsp1^{KO}Acsl4^{KO}, n=7). **(j)** Representative H&E of
999 experiment in (i). Scale bars: 1000µm. **(k)** Overall survival of C57BL/6J male mice with orthotopic
1000 transplantation of isogenic KP, Fsp1^{KO} and Fsp1^{WT} cells with CRISPR/Cas9-mediated knockout
1001 of control (Neo) or Acsl4 (n=5 per group). **(l)** Longitudinal tumor growth (measured via
1002 bioluminescence normalized to first imaging timepoint (day7)) of C57BL/6J mice orthotopically
1003 transplanted with KP, Fsp1^{WT} cells and receiving high (n=6) or low (n=5) VitE diets *ad libitum* 5
1004 days pre-tumor initiation. **(m)** Tumor bioluminescence signal normalized to first imaging
1005 timepoint (day7) of C57BL/6J mice orthotopically transplanted with KP, Fsp1^{KO} cells and
1006 receiving Liproxstatin-1 (LIP1, n=7) or Vehicle (Veh, n=5) daily after tumor establishment. **(n)**
1007 Schematic of KP LUAD GEMMs intratracheally infected with pUSEC lentiviruses containing dual
1008 sgRNAs targeting Fsp1. Mice were dosed with LIP1 (n=6) or Vehicle (Veh, n=6) every other day
1009 starting from tumor initiation. **(o)** Tumor burden of KP LUAD GEMMs with CRISPR/Cas9-
1010 mediated knockout of Fsp1 and treated with Veh or LIP1. **(p)** Representative H&E and 4-HNE
1011 IHC of KP LUAD GEMM tumors with knockout of Fsp1 and treated with Veh or LIP1. Scale
1012 bars: 1000µm. Data are represented as mean values, error bars represent SEM, significance
1013 determined via one-way ANOVA (panel d), two-way ANOVA with Tukey's multiple comparisons
1014 (panels g, i, l, m), two-sided student's t-test (panel o), or Kaplain-Meier simple survival analysis
1015 (panel k). For gel source data, see Supplementary Data 1.
1016
1017 **Extended Data Fig. 7: icFSP1 exerts on-target tumor-suppressive effect**
1018 **(a)** Top: Western blot of KP, Fsp1^{KO} LUAD cells with re-expression of either empty vector (—),
1019 wildtype (WT) hFSP1, or Q319K-mutant hFSP1. Bottom: Representative images of crystal violet
1020 clonogenic assay. **(b)** Cell-TiterGlo Luminescence viability assay of KP, Fsp1^{KO} LUAD cells with

1021 re-expression of either empty vector (—), WT hFSP1, or Q319K-mutant hFSP1. **(c)** CellTiter-Glo
1022 Luminescence viability assay of human or mouse $Fsp1^{WT}$-expressing cells upon RSL3 (0.2μM)
1023 plus increasing concentrations of iFSP1. **(d)** CellTiter-Glo Luminescence viability assay as in (c)
1024 but with FSEN1. **(e)** CellTiter-Glo Luminescence viability assay of human or mouse $Fsp1^{WT}$-
1025 expressing cells upon increasing concentrations of icFSP1. **(f)** CellTiter-Glo Luminescence
1026 viability assay of WT or Q319K-mutant hFSP1-expressing cells upon RSL3 (0.2μM) plus
1027 increasing concentrations of icFSP1. **(g)** Longitudinal tumor growth (measured via
1028 bioluminescence normalized to first imaging timepoint (day7)) in C57BL/6J mice orthotopically
1029 transplanted with isogenic KP, $Fsp1^{KO}$ cells with re-expression of either human FSP1 (hFSP1,
1030 n=5), mouse Fsp1 (mFsp1, n=6), or control (n=6) vector. **(h)** Tumor burden and representative
1031 H&E of KP, $Fsp1^{KO}$ (n=4) and $hFSP1^{WT}$ (n=4) orthotopic lung tumors. Scale bars: 1000μm. **(i)**
1032 Representative H&E of KP, $hFSP1^{WT}$ orthotopic lung tumors from indicated treatment groups.
1033 Scale bar: 2000μm. **(j)** Percent of T cells, alveolar macrophages, interstitial macrophages, and
1034 neutrophils of total CD45+ cells in tumor bearing lungs from mice treated with the indicated
1035 compounds for two weeks (Veh, n=7; LIP1, n=7; icFSP1, n=9; icFSP1+LIP1, n=6). **(k)** Graphical
1036 summary depicting ferroptosis as a barrier to lung cancer, as loss of either Fsp1 or Gpx4 induces
1037 tumor cell ferroptosis and restricts disease progression. **(l)** Summary table of cell lines, their
1038 respective tumor lineage, and mutations where Fsp1 loss resulted in tumor suppression *in vivo*. For
1039 all Cell-TiterGlo assays, n=5 biological replicates per group. Data are represented as mean values,
1040 error bars represent SEM, significance determined via one-way ANOVA with multiple
1041 comparisons (panels g, j) or student's t test (panel h). For gel source data, see Supplementary Data
1042 1.

Fig. 1: Gpx4 loss triggers ferroptosis in lung tumors

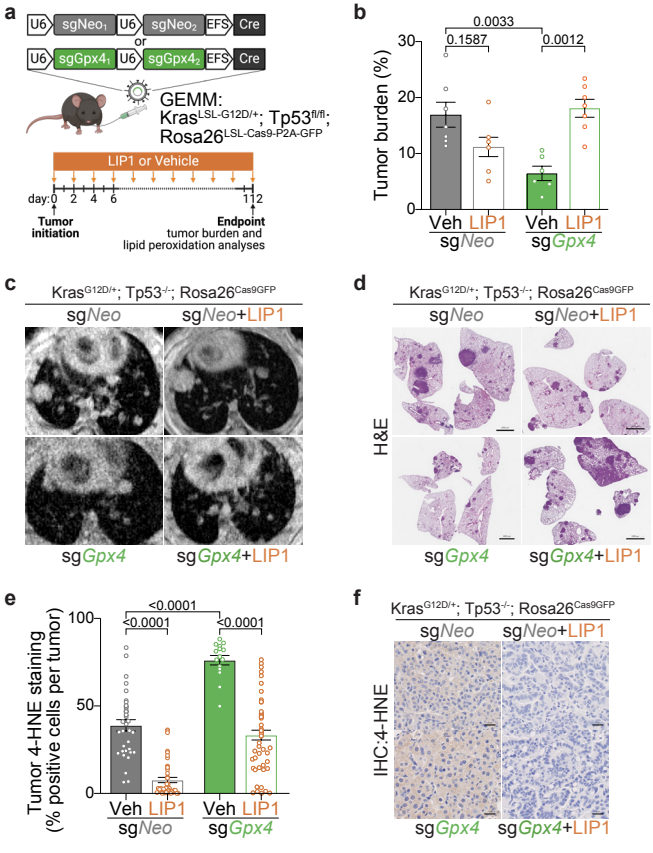

Fig. 2: Fsp1 knockout robustly restricts lung tumorigenesis

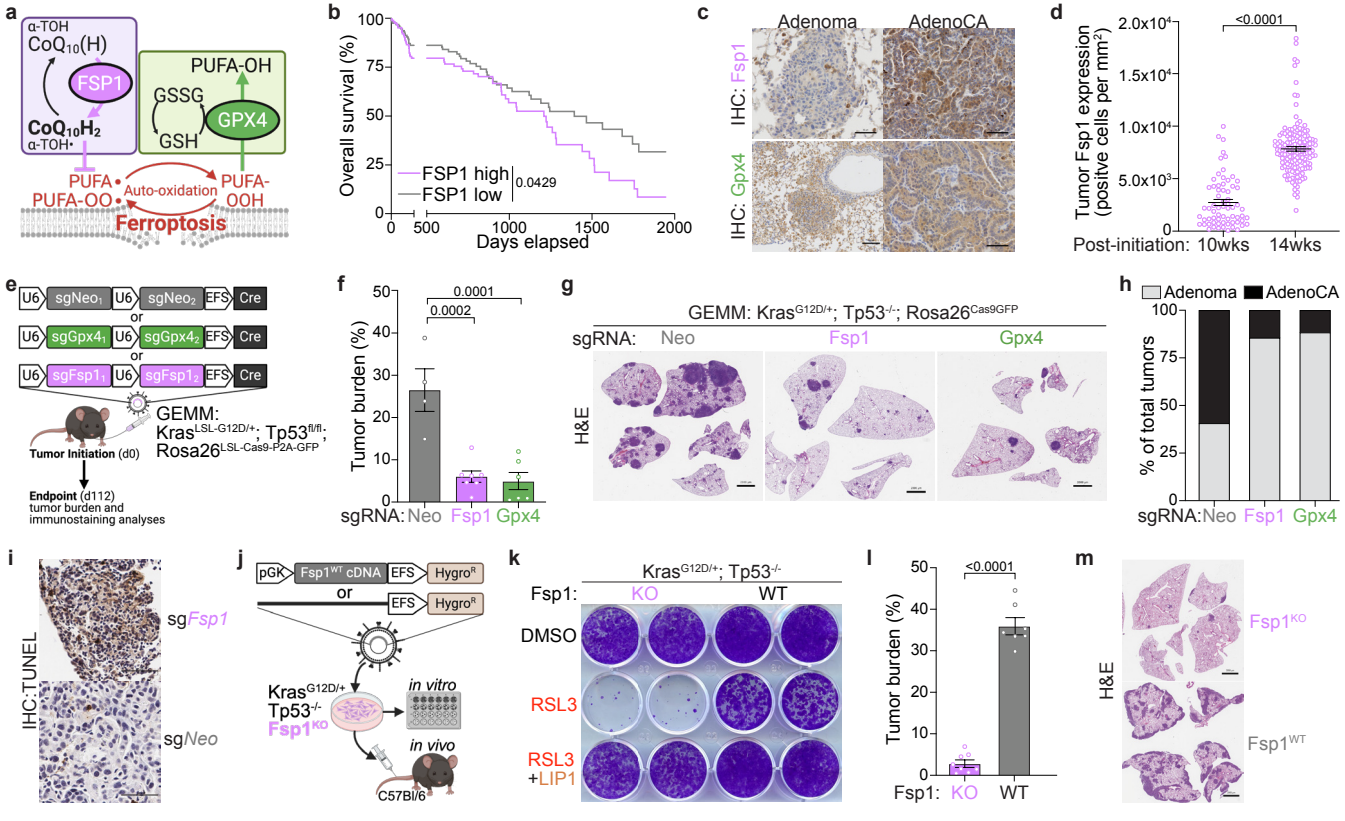

Fig. 3: Sensitivity to FSP1 loss is not dependent on tumor mutations or lineage

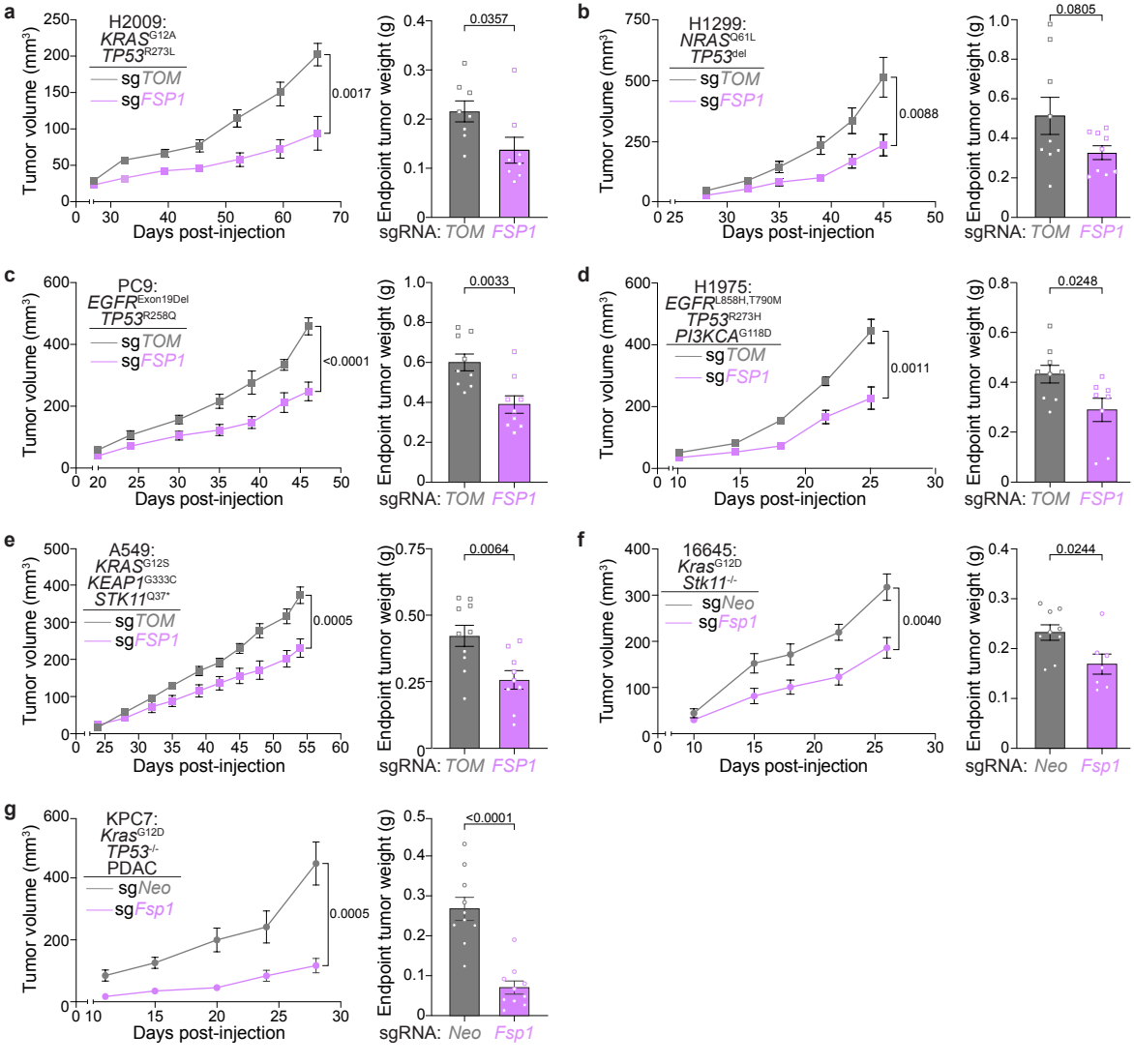

Fig. 4: FSP1 is required for the suppression of ferroptosis *in vivo*

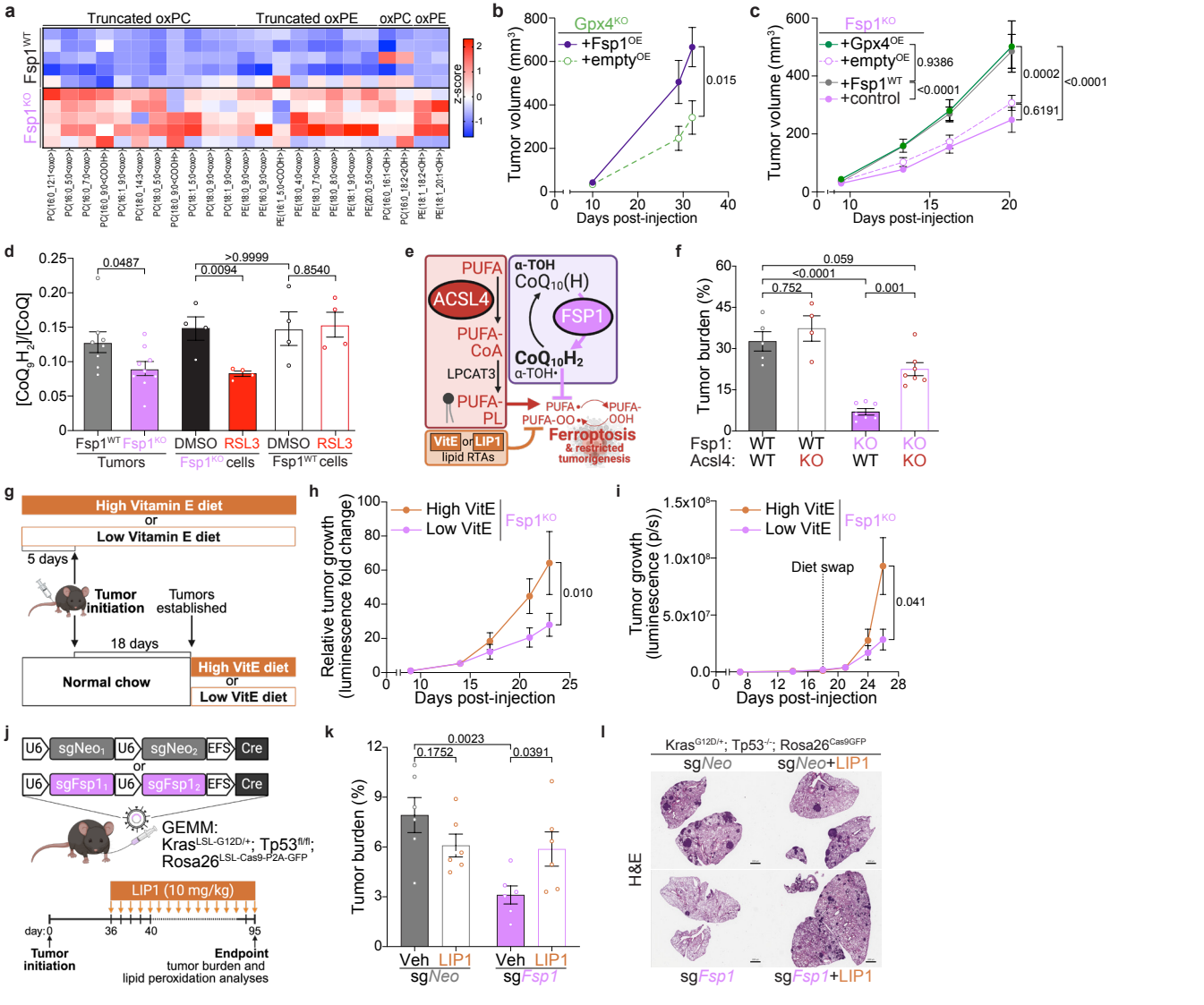

Fig. 5: FSP1 is a viable therapeutic target for *KRAS*-mutant lung adenocarcinoma

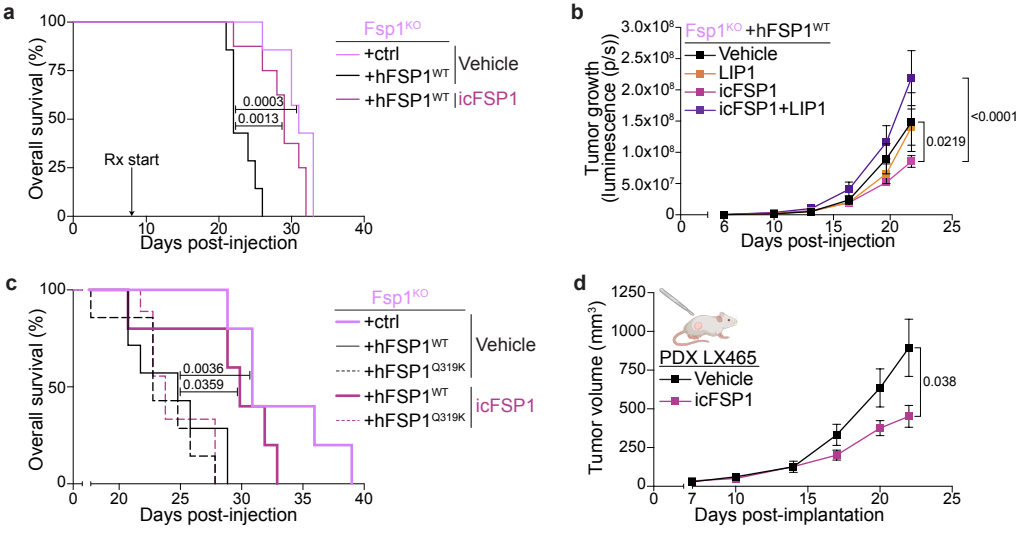

Extended Data Fig. 1: Gpx4 is required by lung cancer cells

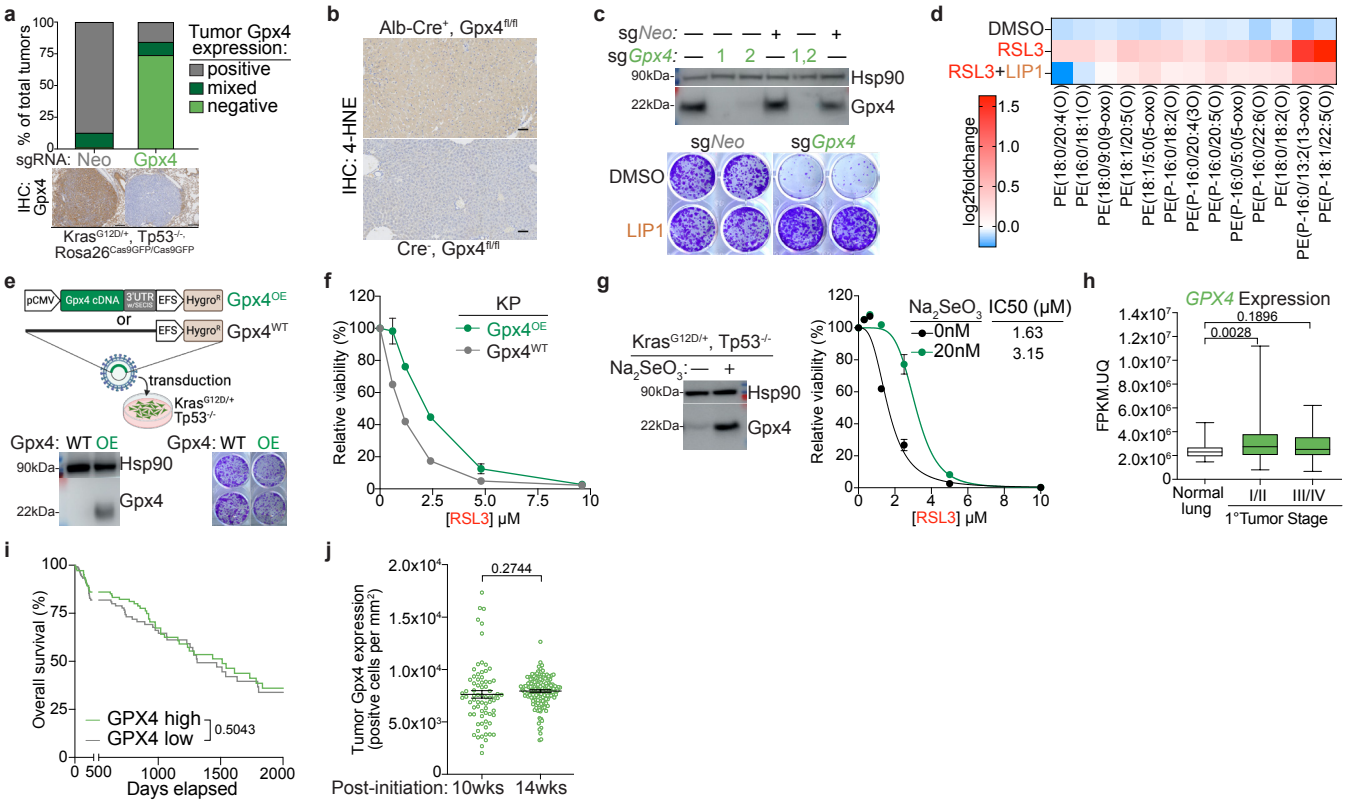

Extended Data Fig. 2: FSP1's anti-ferroptotic function is not dependent on oncogenic signaling

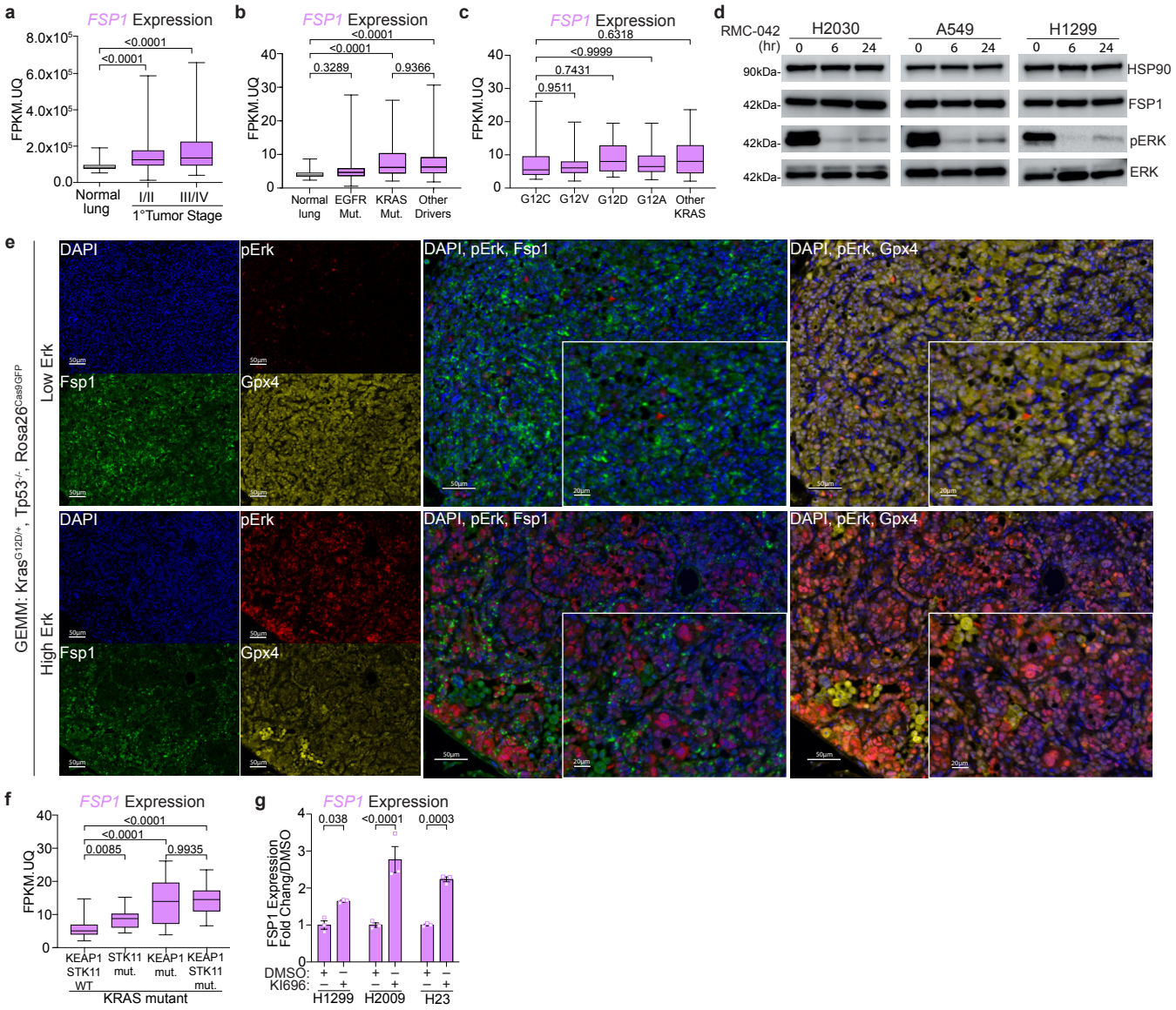

Extended Data Fig. 3: Neither Fsp1 nor Gpx4 have an impact on tumor initiation, proliferation, or apoptosis

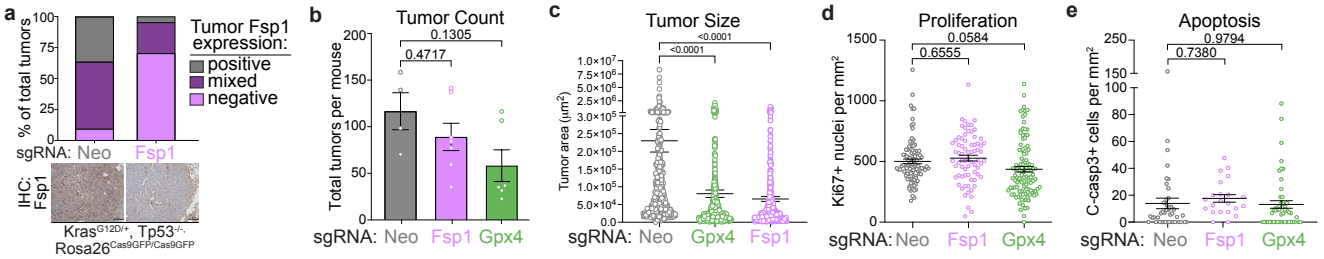

Extended Data Fig. 4: Fsp1 is required for cell-autonomous tumor growth *in vivo*

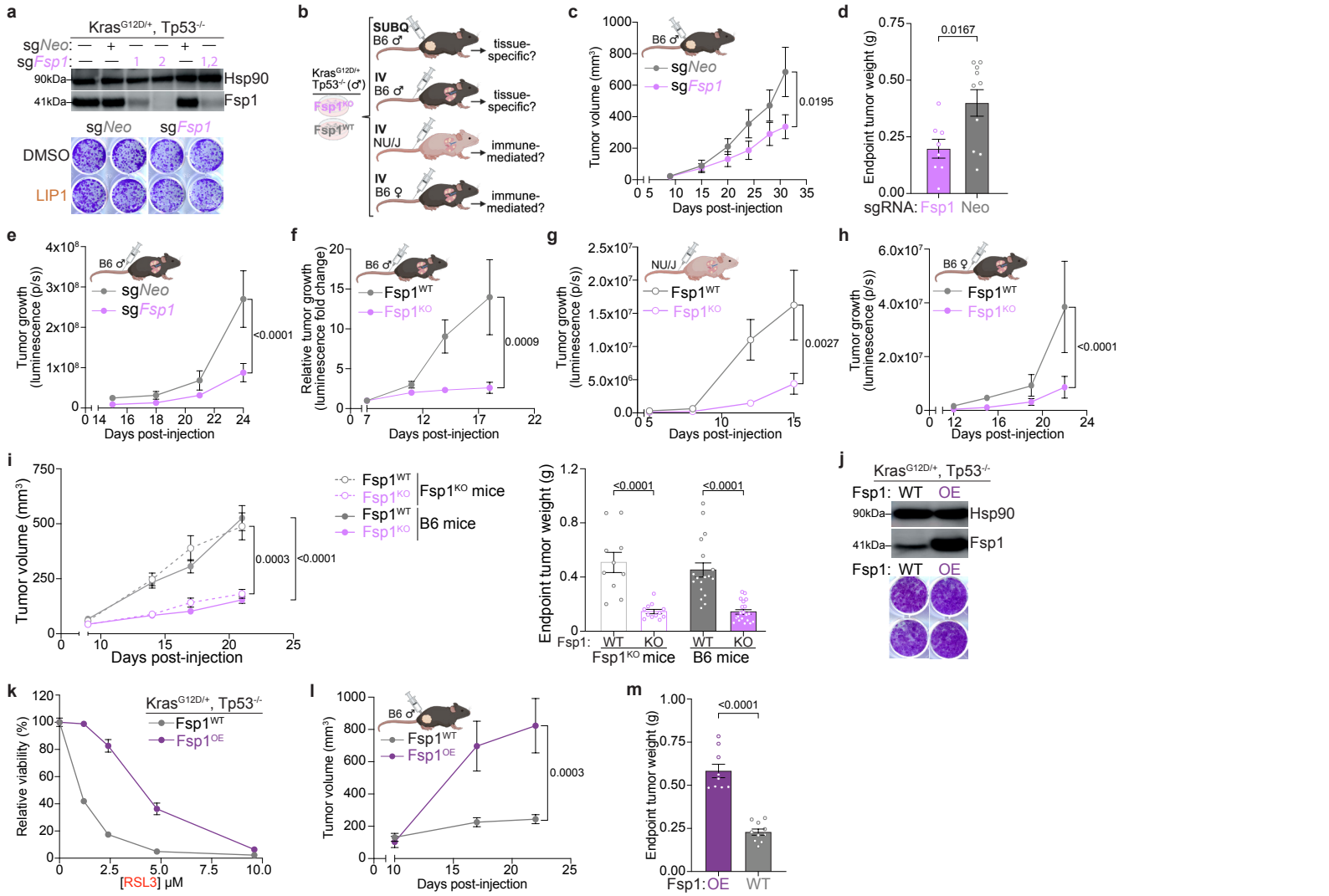

Extended Data Fig. 5: FSP1 loss *in vitro* does not induce ferroptosis without RSL3

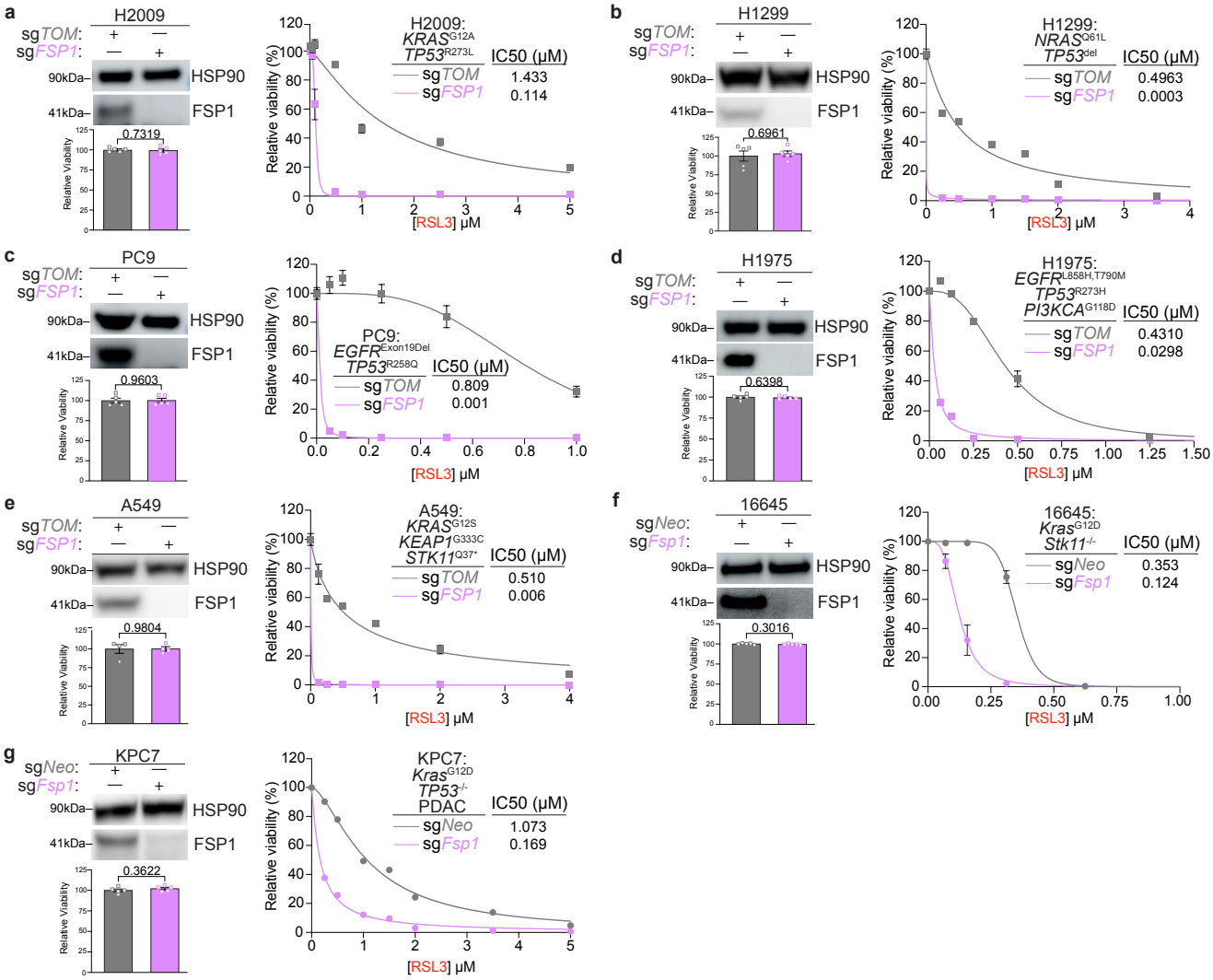

Extended Data Fig. 6: Fsp1 loss promotes tumor cell ferroptosis

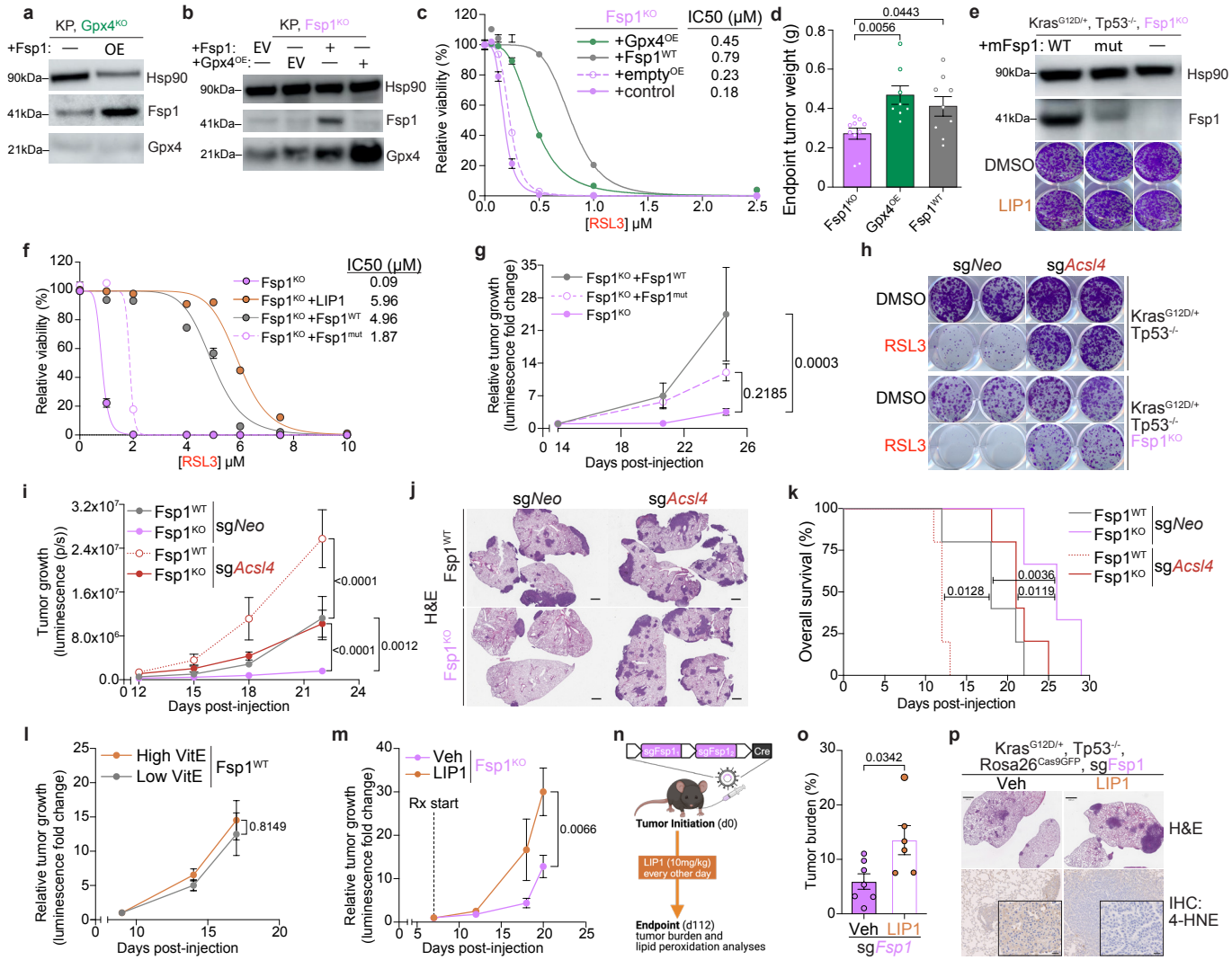

Extended Data Fig. 7: icFSP1 exerts on-target tumor-suppressive effect

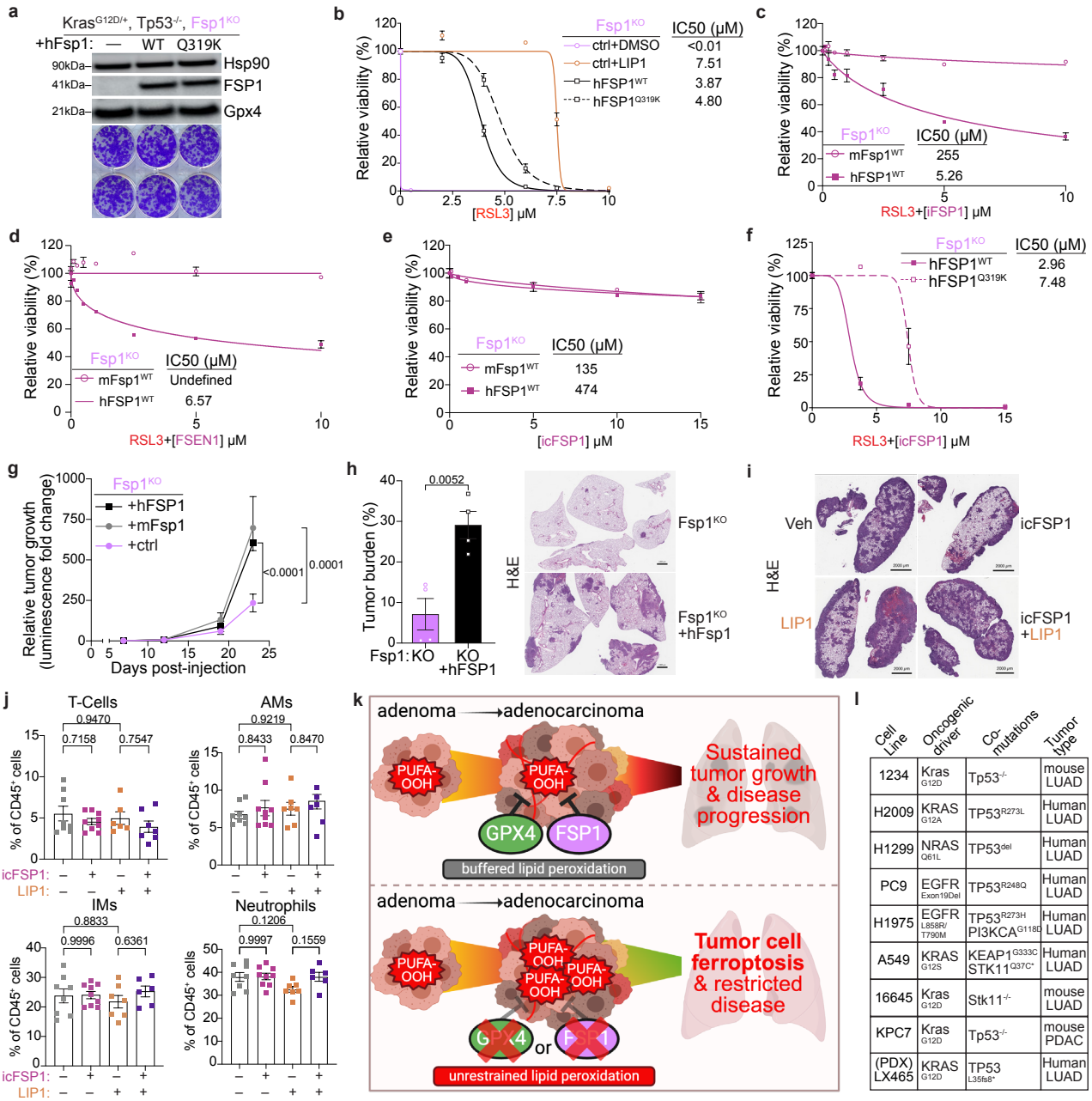

l

Cell Line	Oncogenic driver	Co-mutations	Tumor Type
1234	Kras G12D	Tp53$^{-/-}$	mouse LUAD
H2009	KRAS G12A	TP53^{R273L}	Human LUAD
H1299	NRAS Q61L	TP53^{del}	Human LUAD
PC9	EGFR Exon19Del	TP53^{R248Q}	Human LUAD
H1975	EGFR L858R/ T790M	TP53^{R273H} PI3KCA^{G118D}	Human LUAD
A549	KRAS G12S	KEAP1^{G333C} STK11^{Q37C*}	Human LUAD
16645	Kras G12D	Stk11$^{-/-}$	mouse LUAD
KPC7	Kras G12D	Tp53$^{-/-}$	mouse PDAC
(PDX) LX465	KRAS G12D	TP53 L35fs8*	Human LUAD